Image reconstruction through metamorphosis

Barbara Gris, Chong Chen, Ozan Öktem

Image reconstruction through metamorphosis

Barbara Gris [*] Ozan Öktem [†]

Abstract

This article adapts the framework of metamorphosis to the resolution of inverse problems with shape prior. The metamorphosis framework allows to transform an image via a balance between geometrical deformations and changes in intensities (that can for instance correspond to the appearance of a new structure). The idea developed here is to reconstruct an image from noisy and indirect observations by registering, via metamorphosis, a template to the observed data. Unlike a registration with only geometrical changes, this framework gives good results when intensities of the template are poorly chosen. We show that this method is a well-defined regularization method (proving existence, stability and convergence) and present several numerical examples.

1 Introduction

The paper develops image reconstruction techniques for inverse problems in imaging that are applicable to shape based reconstruction and spatiotemporal imaging.

Shape based reconstruction Some imaging applications focus on recovering the shapes of interior sub-structures of an object whereas variations within these is of less importance. Examples are nano-characterisation of specimens by means of electron microscopy or x-ray phase contrast imaging. As an example, in electron electron tomography (ET) one is often primarily interested in the morphology of sub-cellular structures and nano-characterisation of materials [8]. Another example is quantification of sub-resolution porosity in materials by means of x-ray phase contrast imaging.

In these imaging applications it makes sense to account for qualitative prior shape information during the reconstruction. Enforcing an exact spatial match between a template and the reconstruction is often too strong

[*]LJLL - Laboratoire Jacques-Louis Lions, UPMC, Paris, France.
[†]Department of Mathematics, KTH–Royal Institute of Technology, Stockholm, Sweden.

since realistic shape information is almost always approximate, so the natural approach is to perform reconstruction assuming the structures are 'shape wise similar' to a template.

Spatiotemporal imaging Inverse problems in imaging that involve temporal variation seek to reconstruct time varying spatially distributed quantities, henceforth called images, from noisy time series of measured data. An important sub-class is when all the time dependency in data originates from time dependency of the images that are to be recovered.

This is, e.g., the case in nuclear medical imaging, where techniques like positron emission tomography (PET) and single photon emission computed tomography (SPECT) are used for visualising the distribution of injected radoopharmaceuticals (activity map). The latter is an inherently dynamic quantity, e.g., anatomical structures undergo motion, like the motion of the heart and respiratory motion of the lungs and thoracic wall, during the data acquisition. Not accounting for organ motion is known to degrade the spatial localisation of the radiotracer, leading to spatially blurred images. Furthermore, even when organ motion can be neglected, there are other dynamic processes, such as the uptake and wash-out of radiotracers from body organs. Visualising such kinetics of the radiotracers can actually be a goal in itself, as in pre-clinical imaging studies related to drug discovery/development. The term 'dynamic' in PET and SPECT imaging often refers to such temporal variation due to radiotracers kinetics rather than organ movement [40].

To exemplify the above mentioned issues, consider SPECT based cardiac perfusion studies and $_{18}$F-FDG-PET imaging of lung nodules/tumours. The former needs to account for the beating heart and the latter for respiratory motion of the lungs and thoracic wall. Studies show a maximal displacement of 23 mm (average 15–20 mm) due to respiratory motion [88] and 42 mm (average 8–23 mm) due to cardiac motion in thoracic PET [98].

See section 7 for a more detailed review on various approaches for spatiotemporal image reconstruction in nuclear medicine.

Indirect image registration (matching) A key step in both shape based reconstruction and many reconstruction methods for spatiotemporal imaging is to register a template image so that it matches a target image, which becomes challenging when the template is allowed to undergo non-rigid deformations. As an example, diffeomorphic image registration is an active research area, see [91] for a nice survey Here, the image registration problem is recast as the problem of finding a suitable diffeomorphism that deforms the template into the target image [22]. The underlying assumption is that the target image is contained in the orbit of the template under the group action of diffeomorphisms. This principle can be stated in

a very general setting where diffeomorphism acts on various image features, like landmark points, curves, surfaces, scalar images, or even vector/tensor valued images [100].

The registration problem becomes more challenging when one seeks to *jointly* recover the image and its temporal variation, mainly because the target is only known indirectly through measured data. This is referred to as *indirect image registration* and diffeomorphic image registration can be readily adapted to this setting as shown in [70] for linearised deformations and in [20] for the large deformation diffeomorphic metric mapping (LDDMM) framework.

2 Overview of paper and specific contributions

The paper adapts the metamorphosis framework to the indirect image registration setting. Metamorphosis is an extension of the LDDMM framework where not only the geometry of the template, but also the grey-scale values undergo diffeomorphic changes.

We show how this framework allows to define a regularization method for inverse problems, satisfying properties of existence, stability and convergence. We present several numerical examples for tomographic operators, and in particular give a preliminary result for motion reconstruction when the acquisition is done at several time points. We also study the robustness of our methods with respects to the parameters.

3 Background

3.1 Large diffeomorphic deformations

We recall here the notion of large diffeomorphic deformations defined by flows of time-varying vector fields, as formalized in [3].

Let $\Omega \subset \mathbb{R}^d$ be a fixed bounded domain and let $X := L^2(\Omega, \mathbb{R})$ represent grey scale images on Ω. Next, let V denote a fixed Hilbert space of vector fields on $\mathbb{R}^d$. We will assume $V \subset C_0^p(\Omega)$, i.e., the vector fields are supported on Ω and p times continuously differentiable. Finally, $L^1([0,1], V)$ denotes the space of time-dependent V-vector fields that are integrable, i.e.,

$$\boldsymbol{\nu}(t, \cdot\,) \in V \quad \text{and} \quad t \mapsto \big\|\boldsymbol{\nu}(t, \cdot\,)\big\|_{C^p} \text{ is integrable on } [0,1].$$

Furthermore, we will frequently make use of the following (semi) norm on

$$\|\boldsymbol{\nu}\|_p := \Big(\int_0^1 \big\|\boldsymbol{\nu}(t, \cdot\,)\big\|_V^p \,\mathrm{d}t\Big)^{1/p}$$

where $\|\cdot\|_V$ is the naturally defined norm based upon the inner product of the Hilbert space V of vector fields.

The following proposition allows one to consider flows of elements in $L^1([0,1],V)$ and ensures that these flows belong to $\mathrm{Diff}_0^p(\Omega)$ (set of p-diffeomorphisms that are supported in $\Omega \subset \mathbb{R}^d$, and if Ω is unbounded, tend to zero towards infinity).

Proposition 1. *Let $\boldsymbol{\nu} \in L^1([0,1],V)$ and consider the ordinary differential equation (flow equation):*

$$\begin{cases} \dfrac{\mathrm{d}}{\mathrm{d}t}\phi(t,x) = \boldsymbol{\nu}\big(t,\phi(t,x)\big) \\ \phi(0,x) = x \end{cases} \qquad \text{for any } x \in \Omega \text{ and } t \in [0,1]. \tag{1}$$

Then, (1) has a unique absolutely continuous solution $\phi(t,\,\cdot\,) \in \mathrm{Diff}_0^p(\mathbb{R}^d)$.

The above result is proved in [3] and the unique solution of (1) is henceforth called the *flow of* $\boldsymbol{\nu}$. We also introduce to notation $\varphi_{s,t}^{\boldsymbol{\nu}} \colon \mathbb{R}^d \to \mathbb{R}^d$ that refers to

$$\varphi_{s,t}^{\boldsymbol{\nu}} := \phi(t,\,\cdot\,) \circ \phi(s,\,\cdot\,)^{-1} \quad \text{for } s,t \in [0,1] \tag{2}$$

where $\phi \colon \Omega \to \mathbb{R}^d$ denotes the unique solution to (1).

As stated next, the set of diffeomorphisms that are given as flows forms a group that is a complete metric space [3].

Proposition 2. *Let $V \subset C_0^p(\Omega)$ ($p \geq 1$) be an admissible reproducing kernel Hilbert space (RKHS) and define*

$$G_V := \Big\{ \phi \colon \mathbb{R}^d \to \mathbb{R}^d \mid \phi = \varphi_{0,1}^{\boldsymbol{\nu}} \text{ for some } \boldsymbol{\nu} \in L^2([0,1],V) \Big\}.$$

Then G_V forms a sub-group of $\mathrm{Diff}_0^p(\mathbb{R}^d)$ and

$$\begin{aligned} \mathrm{d}_{\mathrm{G}}(\phi_1,\phi_2) &:= \inf\Big\{ \|\boldsymbol{\nu}\|_1 : \boldsymbol{\nu} \in L^1([0,1],V) \text{ and } \phi_1 = \phi_2 \circ \varphi_{0,1}^{\boldsymbol{\nu}} \Big\} \\ &= \inf\Big\{ \|\boldsymbol{\nu}\|_2 : \boldsymbol{\nu} \in L^1([0,1],V) \text{ and } \phi_1 = \phi_2 \circ \varphi_{0,1}^{\boldsymbol{\nu}} \Big\} \end{aligned}$$

defines a metric on G_V.

The elements of G_V are called *large diffeomorphic deformations* and G_V acts on X via the *geometric group action* that is defined by the operator

$$\mathcal{W} \colon G_V \times X \to X \quad \text{where} \quad \mathcal{W}(\phi, I_0) := I_0 \circ \phi^{-1}. \tag{3}$$

We conclude by stating regularity properties of flows of velocity fields as well as the group action in (3), these will play an important role in what is to follow. The proof is given in [14].

Proposition 3. *Assume $V \subset C_0^p(\Omega)$ ($p \geq 1$) is a fixed admissible Hilbert space of vector fields on Ω and $\{\boldsymbol{\nu}^n\}_n \subset L^2([0,1],V)$ a sequence that converges weakly to $\boldsymbol{\nu} \in L^2([0,1],V)$. Then, the following holds with $\varphi_t^n := \varphi_{0,t}^{\boldsymbol{\nu}^n}$:*

1. $(\varphi_t^n)^{-1}$ *converges to* $(\varphi_{0,t}^{\boldsymbol{\nu}})^{-1}$ *uniformly w.r.t.* $t \in [0,1]$ *and uniformly on compact subsets of* $\Omega \subset \mathbb{R}^d$.

2. $\lim_{n\to\infty} \left\| \mathcal{W}(\varphi_t^n, I_0) - \mathcal{W}(\varphi_{0,t}^{\boldsymbol{\nu}}, I_0) \right\|_X = 0$ *for any* $f \in X$.

4 Image registration

Image registration (matching) refers to the task of deforming a given template image $I_0 \in X$ so that it matches a given target image $I^* \in X$.

The above task can also be stated in an *indirect* setting, which refers to the case when the template $I_0 \in X$ is to be registered against a target $I^* \in X$ that is only indirectly known through data $g \in Y$ where

$$g = \mathcal{A}(I^*) + e. \tag{4}$$

In the above, $\mathcal{A}\colon X \to Y$ (forward operator) is known and assumed to be differentiable and $e \in Y$ is a single sample of a Y-valued random element that denotes the measurement noise in the data.

A further development requires specifying what is meant by deforming a template image, and we will henceforth consider diffeomorphic (non-rigid) deformations, i.e., diffeomorphisms that deform images by actin g on them through a group action.

4.1 LDDMM-based registration

An example of using large diffeomorphic (non-rigid) deformations for image registration is to minimize the following functional:

$$G_V \ni \phi \mapsto \frac{\gamma}{2} \mathrm{d}_{\mathrm{G}}(\mathrm{Id}, \phi)^2 + \left\| \mathcal{W}(\phi, I_0) - I^* \right\|_X^2 \quad \text{given } \gamma > 0.$$

If V is admissible, then minimizing the above functional on G_V amounts to minimizing the following functional on $L^2([0,1], V)$ [100, Theorem 11.2 and Lemma 11.3]:

$$L^2([0,1], V) \ni \boldsymbol{\nu} \mapsto \frac{\gamma}{2} \|\boldsymbol{\nu}\|_2^2 + \left\| \mathcal{W}(\varphi_{0,1}^{\boldsymbol{\nu}}, I_0) - f \right\|_X^2 \quad \text{given } \gamma > 0.$$

Such a reformulation is advantageous since $L^2([0,1], V)$ is a vector space, whereas G_V is not, so it is easier to minimize a functional over $L^2([0,1], V)$ rather than over G_V.

The above can be extended to the indirect setting as shown in [20], which we henceforth refer to as *LDDMM-based indirect registration*. More precisely, the corresponding indirect registration problem can be adressed by minimising the functional

$$L^2([0,1], V) \ni \boldsymbol{\nu} \mapsto \frac{\gamma}{2} \|\boldsymbol{\nu}\|_2^2 + \mathcal{L}\big((\mathcal{A} \circ \mathcal{W})(\varphi_{0,t}^{\boldsymbol{\nu}}, I_0), g\big).$$

Here, $\mathcal{L}\colon Y \times Y \to \mathbb{R}$ is typically given by an appropriate affine transform of the data negative log-likelihood [6], so minimizing $f \mapsto \mathcal{L}\big(\mathcal{A}(f), g\big)$ corresponds to seeking a maximum likelihood solution of (4).

An interpretation of the above is that the template image I_0, which is assumed to be given a priori, acts as a *shape prior* when solving the inverse problem in (4) and $\gamma > 0$ is a regularization parameter that governs the influence of this shape priori against the need to fit measured data. This interpretation becomes more clear when one re-formulates LDDMM-based indirect registration as

$$\begin{cases} \min\limits_{\boldsymbol{\nu} \in L^2([0,1],V)} \left[\dfrac{\gamma}{2} \|\boldsymbol{\nu}\|_2^2 + \mathcal{L}\Big((\mathcal{A} \circ \mathcal{W})\big(\phi(1,\ \cdot\ ), I_0\big), g \Big) \right] \\ \dfrac{d}{dt}\phi(t,x) = \boldsymbol{\nu}\big(t, \phi(t,x)\big) \quad (t,x) \in \Omega \times [0,1], \\ \phi(0,x) = x \quad x \in \Omega. \end{cases} \tag{5}$$

5 Metamorphosis-based indirect registration

5.1 Motivation

As shown in [20], access to a template that can act as a shape prior can have profound effect in solving challenging inverse problem in imaging. As an example, tomographic imaging problems that are otherwise intractable (highly noisy and sparsely sampled data) can be successfully addressed using indirect registration even when using a template is far from the ground truth image used for generating the data.

When template has correct topology and intensity levels, then LDDMM-based indirect registration with geometric group action is remarkably stable as shown in [20]. Using a geometric group action, however, makes it impossible to create or remove intensity, e.g., it is not possible to start out from a template with a single isolated structure and deform it to a image with two isolated structures. This severely limits the usefulness of LDDMM-based indirect registration, e.g., spatiotemporal images (moves) are likely to involve changes in both geometry (objects appear or disappear) and intensity. See fig. 1 for an example of how wrong intensity influences the registration.

As noted in [20], one approach is to replace the geometric group action with one that alters intensities, e.g., a mass preserving group action. Another is to keep the geometric group action, but replace LDDMM with a framework for diffeomorphic deformations that acts on both geometry and intensities, e.g., metamorphosis. This latter approach is the essence of metamorphosis-based indirect registration.

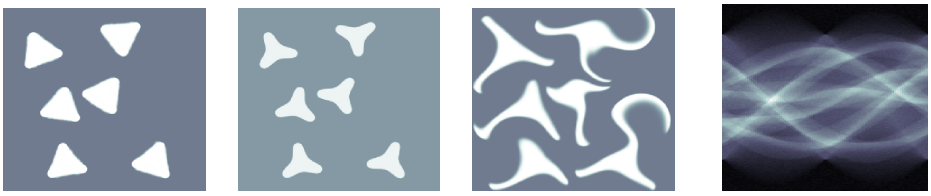

(a) Template. (b) Target. (c) Reconstruction. (d) Data.

Figure 1: Reconstruction by LDDMM-based indirect registration (c) using a template (a) with a geometry that matches the target (b), but with incorrect background intensity values. Target is observed indirectly through tomographic data (d), which is 2D parallel beam Radon transform with 100 evenly distributed directions (see section 6.1 for details). The artefacts in the reconstruction are due to incorrect background intensity in template.

5.2 Metamorphosis

In metamorphosis diffeomorphisms are still generated by flows as in LDDMM, but the difference is that they now act with a geometric group action on *both* intensities and underlying points. As such, metamorphosis extends LDDMM. The abstract definition of a metamorphosis reads as follows.

Definition 1 (Metamorphosis [96])**.** *Let $V \subset C_0^p(\Omega)$ be an admissible Hilbert space and "$\cdot$" denotes some group action of G_V on X. A* Metamorphosis *is a curve $t \mapsto (\phi_t, f_t)$ in $G_V \times X$. The curve $t \mapsto f_t := \phi_t.f_t$ is called the* image *part, $t \mapsto \phi_t$ is the* deformation *part, and $t \mapsto f_t$ is the* template *part.*

The image part represents the temporal evolution that is not related to intensity changes, i.e., evolution of underlying geometry, whereas the template part is the evolution of the intensity. Both evolutions, which are combined in metamorphosis, are driven by the same underlying flow of diffeomorphisms in G_V.

A important case is when the metamorphosis $t \mapsto (\phi_t, f_t)$ has a deformation part that solves the flow equation (1) and a template part is C^1 in time. More precisely, $L^2([0,1], X)$ denotes the space of functions in X that are square integrable, i.e.,

$$\zeta(t, \cdot) \in X \quad \text{and} \quad t \mapsto \left\|\zeta(t, \cdot)\right\|_X \text{ is in } L^2([0,1], \mathbb{R}).$$

The norm on $L^2([0,1], X)$ is then

$$\|\zeta\|_2 := \left(\int_0^1 \left\|\zeta(t, \cdot)\right\|_X^2 \mathrm{d}t\right)^{1/2}.$$

We will also use the notation

$$L^2([0,1], V \times X) := L^2([0,1], V) \times L^2([0,1], X).$$

Bearing in mind the above notation, for given $(\boldsymbol{\nu}, \zeta) \in L^2([0,1], V \times X)$ and $I_0 \in X$, define the curve $t \mapsto I_t^{\boldsymbol{\nu},\zeta}$, which is absolutely continuous on $[0,1]$, as the solution to

$$\begin{cases} \dfrac{\mathrm{d}}{\mathrm{d}t} I_t^{\boldsymbol{\nu},\zeta}(x) = \zeta\big(t, \varphi_{0,t}^{\boldsymbol{\nu}}(x)\big) \\ I_0^{\boldsymbol{\nu},\zeta}(x) = I_0(x) \end{cases} \qquad \text{with } \varphi_{0,t}^{\boldsymbol{\nu}} \in G_V \text{ as in (2).} \tag{6}$$

The metamorphosis can now be parametrised as $t \mapsto (\varphi_{0,t}^{\boldsymbol{\nu}}, I_t^{\boldsymbol{\nu},\zeta})$.

Indirect registration The indirect registration problem in section 4 can be approached by metamorphosis instead of LDDMM. Analogous to LDDMM-based indirect image registration in [20], we define *metamorphosis-based indirect image registration* as the minimization of the objective functional

$$\mathcal{J}_{\gamma,\tau}(\,\cdot\,; g) \colon L^2([0,1], V \times X) \to \mathbb{R}$$

defined as

$$\mathcal{J}_{\gamma,\tau}(\boldsymbol{\nu}, \zeta; g) := \frac{\gamma}{2}\|\boldsymbol{\nu}\|_2^2 + \frac{\tau}{2}\|\zeta\|_2^2 + \mathcal{L}\Big(\mathcal{A}\big(\mathcal{W}(\varphi_{0,1}^{\boldsymbol{\nu}}, I_1^{\boldsymbol{\nu},\zeta})\big), g\Big) \tag{7}$$

for given regularization parameters $\gamma, \tau \geq 0$, measured data $g \in Y$, and initial template $I_0 \in X$ that sets the initial condition $I_0^{\boldsymbol{\nu},\zeta}(x) := I_0(x)$.

Hence, performing metamorphosis-based indirect image registration of a template I_0 against a target indirectly observed through data g amounts to solving

$$(\widehat{\boldsymbol{\nu}}, \widehat{\zeta}) \in \operatorname*{arg\,min}_{(\boldsymbol{\nu},\zeta)} \mathcal{J}_{\gamma,\tau}(\boldsymbol{\nu}, \zeta; g).$$

The above always has a solution assuming the data discrepancy and the forward operator fulfills some weak requirements (see proposition 4). From a solution we then obtain the following:

- *Initial template:* $I_0 \in X$ such that $I_0^{\boldsymbol{\nu},\zeta} := I_0$.
- *Reconstruction:* $f_1^{\widehat{\boldsymbol{\nu}},\widehat{\zeta}} = \mathcal{W}\big(\varphi_{0,1}^{\widehat{\boldsymbol{\nu}}}, I_1^{\widehat{\boldsymbol{\nu}},\widehat{\zeta}}\big) \in X$, the final registered template.
- *Image trajectory:* $t \mapsto \mathcal{W}\big(\varphi_{0,t}^{\widehat{\boldsymbol{\nu}}}, I_t^{\widehat{\boldsymbol{\nu}},\widehat{\zeta}}\big)$, the evolution of both geometry and intensity of the template.
- *Intensity trajectory:* $t \mapsto I_t^{\widehat{\boldsymbol{\nu}},\widehat{\zeta}}$, is the evolution of intensities of the template, i.e., the part that does not include evolution of geometry.
- *Deformation trajectory:* $t \mapsto \mathcal{W}(\varphi_{0,t}^{\widehat{\boldsymbol{\nu}}}, I_0)$, is the geometric evolution of the template, i.e., the part that does not include evolution of intensity.

5.3 Regularising properties

In the following we prove several properties (existence, stability and convergence) of metamorphosis-based indirect image registration, which are necessary if the approach is to constitute a *well defined regularisation method* (notion defined in [35]). We set $X := L^2(\Omega, \mathbb{R})$ and Y a Hilbert space.

Proposition 4 (Existence)**.** *Assume $\mathcal{A}\colon X \to Y$ is continuous and the data discrepancy $\mathcal{L}(\,\cdot\,, g)\colon Y \to \mathbb{R}$ is weakly lower semi-continuous for any $g \in Y$. Then, $\mathcal{J}_{\gamma,\tau}(\,\cdot\,, g)\colon L^2([0,1], V \times X) \to \mathbb{R}$ defined through (6) and (7) has a minimizer in $L^2([0,1], V \times X)$ for any $I_0 \in L^2(\Omega, \mathbb{R})$.*

Proof. We follow here the strategy to prove existence of minimal trajectories for metamorphosis (as in [19] for instance). One considers a minimizing sequence of $\mathcal{J}_{\gamma,\tau}(\,\cdot\,; g)$, i.e., a sequence that converges to the infimum of $\mathcal{J}_{\gamma,\tau}(\,\cdot\,; g)$ (such a sequence always exists). The idea is to prove that such a minimizing sequence has a sub-sequence that converges to a point in $L^2([0,1], V \times X)$, i.e., the infimum is contained in $L^2([0,1], V \times X)$ which proves existence of a minima.

Bearing in mind the above, we start by considering a minimizing sequence $\{(\boldsymbol{\nu}^n, \zeta^n)\}_n \subset L^2([0,1], V \times X)$ to $\mathcal{J}_{\gamma,\tau}(\,\cdot\,; g)$, i.e.,

$$\lim_{n\to\infty} \mathcal{J}_{\gamma,\tau}(\boldsymbol{\nu}^n, \zeta^n; g) = \inf_{\boldsymbol{\nu},\zeta} \mathcal{J}_{\gamma,\tau}(\boldsymbol{\nu}, \zeta; g).$$

Since $\{\boldsymbol{\nu}^n\}_n \subset L^2([0,1], V)$ is bounded, it has a sub-sequence that converges to an element $\boldsymbol{\nu}^\infty \in L^2([0,1], V)$. Likewise, $\{\zeta^n\}_n \subset L^2([0,1], X)$ has a sub-sequence that converges to an element $\zeta^\infty \in L^2([0,1], X)$. Hence, with a slight abuse of notation, we conclude that

$$\boldsymbol{\nu}^n \rightharpoonup \boldsymbol{\nu}^\infty \quad \text{and} \quad \zeta^n \rightharpoonup \zeta^\infty \quad \text{as } n \to \infty.$$

The aim is now to prove existence of minimizers by showing that $(\boldsymbol{\nu}^\infty, \zeta^\infty)$ is a minimizer to $\mathcal{J}_{\gamma,\tau}(\,\cdot\,; g)\colon L^2([0,1], V \times X) \to \mathbb{R}$.

Before proceeding, we introduce some notation in order to simplify the expressions. Define

$$I_t^n := I_t^{\boldsymbol{\nu}^n, \zeta^n} \quad \text{and} \quad \varphi_{s,t}^n := \varphi_{s,t}^{\boldsymbol{\nu}^n} \quad \text{for } n \in \mathbb{N} \bigcup \{\infty\}. \tag{8}$$

Hence, assuming geometric group action (3) and using (2), we can write

$$\mathcal{J}_{\gamma,\tau}(\boldsymbol{\nu}^n, \zeta^n; g) = \frac{\gamma}{2}\|\boldsymbol{\nu}^n\|_2^2 + \frac{\tau}{2}\|\zeta^n\|_2^2 + \mathcal{L}\Big(\mathcal{A}\big(I_1^n \circ \varphi_{1,0}^n\big), g\Big)$$

for $n \in \mathbb{N} \bigcup \{\infty\}$. Assume next that the following holds:

$$I_1^n \circ \varphi_{1,0}^n \rightharpoonup I_1^\infty \circ \varphi_{1,0}^\infty \quad \text{as } n \to \infty. \tag{9}$$

The data discrepancy term $\mathcal{L}(\,\cdot\,, g)\colon Y \to \mathbb{R}$ is weakly lower semi continuous and the forward operator $\mathcal{A}\colon X \to Y$ is continuous, so $\mathcal{L}(\,\cdot\,, g) \circ \mathcal{A}$ is also weakly lower semi continuous and then (9) implies

$$\mathcal{L}\big(\mathcal{A}(I_1^\infty \circ \varphi_{1,0}^\infty), g\big) \leq \liminf_{n\to\infty} \mathcal{L}(\mathcal{A}(I_1^n \circ \varphi_{1,0}^n), g). \tag{10}$$

Furthermore, from the weak convergences of $\boldsymbol{\nu}^n$ and ζ^n, we get

$$\frac{\gamma}{2}\|\boldsymbol{\nu}^\infty\|_2^2 + \frac{\tau}{2}\|\zeta^\infty\|_2^2 \leq \liminf_{n\to\infty}\Big[\frac{\gamma}{2}\|\boldsymbol{\nu}^n\|_2^2 + \frac{\tau}{2}\|\zeta^n\|_2^2\Big]. \tag{11}$$

Hence, combining (10) and (11) we obtain

$$\mathcal{J}_{\gamma,\tau}(\boldsymbol{\nu}^\infty, \zeta^\infty; g) \leq \lim_{n\to\infty} \mathcal{J}_{\gamma,\tau}(\boldsymbol{\nu}^n, \zeta^n; g).$$

Since $\big\{(\boldsymbol{\nu}^n, \zeta^n)\big\}_n \subset L^2\left([0,1], V \times X\right)$ is a minimizing sequence, this yields

$$\mathcal{J}_{\gamma,\tau}(\boldsymbol{\nu}^\infty, \zeta^\infty; g) = \inf_{(\boldsymbol{\nu},\zeta)\in L^2([0,1],V\times X)} \mathcal{J}_{\gamma,\tau}(\boldsymbol{\nu}, \zeta; g),$$

which proves $(\boldsymbol{\nu}^\infty, \zeta^\infty) \in L^2\left([0,1], V \times X\right)$ is a minimizer to $\mathcal{J}_{\gamma,\tau}(\,\cdot\,; g)$.

Hence, to finalize the proof we need to show that (9) holds. We start by observing that the solution of (6) can be written as

$$I_t^n := I_0^n(x) + \int_0^t \zeta^n\big(s, \varphi_{0,s}^n(x)\big)\mathrm{d}s \quad \text{for } n \in \mathbb{N} \cup \{\infty\}, \tag{12}$$

and note that $(t,x) \mapsto I_t^n(x) \in C([0,1] \times \Omega, \mathbb{R})$. Next, we claim that

$$I_1^n \rightharpoonup I_1^\infty \quad \text{for some } I_1^\infty \in X,$$

which is equivalent to

$$\lim_{n\to\infty} \langle I_1^n - I_1^\infty, J\rangle = 0 \quad \text{for any } J \in L^2(\Omega, \mathbb{R}). \tag{13}$$

To prove (13), note first that since continuous functions are dense in L^2, it is enough to show (13) holds for $J \in C_0(\Omega, \mathbb{R})$. Next,

$$\langle I_1^n - I_1^\infty, J\rangle = \int_\Omega \int_0^t \Big(\zeta^n\big(s, \varphi_{0,s}^n(x)\big) - \zeta^\infty\big(s, \varphi_{0,s}^\infty(x)\big)\Big) J(x)\mathrm{d}s\mathrm{d}x \tag{14}$$

$$= \int_\Omega \int_0^t \Big(\zeta^n\big(s, \varphi_{0,s}^n(x)\big) - \zeta^n\big(s, \varphi_{0,s}^\infty(x)\big)\Big) J(x)\mathrm{d}s\mathrm{d}x \tag{15}$$

$$+ \int_\Omega \int_0^t \Big(\zeta^n\big(s, \varphi_{0,s}^n(x)\big) - \zeta^\infty\big(s, \varphi_{0,s}^\infty(x)\big)\Big) J(x)\mathrm{d}s\mathrm{d}x. \tag{16}$$

Let us now take a closer look at the term in (15):

$$\begin{aligned}
&\int_\Omega \int_0^t \Big(\zeta^n\big(s, \varphi^n_{0,s}(x)\big) - \zeta^n\big(s, \varphi^\infty_{0,s}(x)\big)\Big) J(x) \mathrm{d}s\mathrm{d}x \\
&\quad = \int_\Omega \int_0^t \zeta^n(s,x) J\big(\varphi^n_{0,s}(x)\big) \big|D\varphi^n_{0,s}(x)\big| \mathrm{d}s\mathrm{d}x \\
&\qquad\qquad - \int_\Omega \int_0^t \zeta^\infty(s,x) J\big(\varphi^\infty_{0,s}(x)\big) \big|D\varphi^\infty_{0,s}(x)\big| \mathrm{d}s\mathrm{d}x \\
&\quad = \int_\Omega \int_0^t \zeta^n(s,x) \Big(J\big(\varphi^n_{0,s}(x)\big) \big|D\varphi^n_{0,s}(x)\big| - J\big(\varphi^\infty_{0,s}(x)\big) \big|D\varphi^\infty_{0,s}(x)\big|\Big) \mathrm{d}s\mathrm{d}x \\
&\qquad - \int_\Omega \int_0^t \Big(\zeta^\infty(s,x) - \zeta^n(s,x)\Big) J\big(\varphi^\infty_{0,s}(x)\big) \big|D\varphi^\infty_{0,s}(x)\big| \mathrm{d}s\mathrm{d}x \\
&\qquad\qquad\qquad\qquad = \langle \zeta^n, J^n - J^\infty \rangle - \langle \zeta^\infty - \zeta^n, J^\infty \rangle
\end{aligned}$$

where $J^n \in L^2\left([0,1], X\right)$ is defined as

$$J^n(s,x) := J\big(\varphi^n_{s,0}(x)\big) \big|D\varphi^n_{s,0}(x)\big| \quad \text{for } n \in \mathbb{N} \bigcup \{\infty\}. \tag{17}$$

By proposition 3 we know that $\varphi^n_{s,0} \to \varphi^\infty_{s,0}$ and $D\varphi^n_{s,0} \to D\varphi^\infty_{s,0}$ uniformly on Ω. Since J is continuous on Ω, we conclude that $\|J^n - J^\infty\|_2$ tends to 0. Since ζ^n is bounded, we conclude that

$$\langle \zeta^n, J^n - J^\infty \rangle \leq \|\zeta^n\|_2 \cdot \|J^n - J^\infty\|_2 \to 0.$$

Furthermore, since $\zeta^n \rightharpoonup \zeta^\infty$, we also get $\langle \zeta^\infty - \zeta^n, J^\infty \rangle \to 0$. Hence, we have shown that (15) tends to zero, i.e.,

$$\lim_{n\to\infty} \int_\Omega \int_0^t \Big(\zeta^n\big(s, \varphi^n_{0,s}(x)\big) - \zeta^n\big(s, \varphi^\infty_{0,s}(x)\big)\Big) J(x) \mathrm{d}s\mathrm{d}x = 0.$$

Finally, we consider the term in (16). Since $\zeta^n \rightharpoonup \zeta^\infty$, we immediately obtain

$$\int_\Omega \int_0^t \Big(\zeta^n\big(s, \varphi^\infty_s(x)\big) - \zeta^\infty\big(s, \varphi^\infty_s(x)\big)\Big) J(x) \mathrm{d}s\mathrm{d}x = \big\langle \zeta^n - \zeta^\infty, J^\infty \big\rangle \to 0.$$

To summarise, we have just proved that both terms (15) and (16) tend to 0 as $n \to \infty$, which implies that (13) holds, i.e., $I^n_1 \rightharpoonup I^\infty_1$.

To prove (9), i.e., $I^n_1 \circ \varphi^n_{1,0} \rightharpoonup I^\infty_1 \circ \varphi^\infty_{1,0}$, we need to show that

$$\lim_{n\to\infty} \big\langle I^n_1 \circ \varphi^n_{1,0} - I^\infty_1 \circ \varphi^\infty_{1,0}, J \big\rangle = 0 \quad \text{for any } J \in L^2(\Omega, \mathbb{R}), \tag{18}$$

and as before, we may assume $J \in C_0(\Omega, \mathbb{R})$. Using (17) we can express the term in (18) whose limit we seek as

$$\begin{aligned}
&\big|\langle I^n_1 \circ \varphi^n_{1,0} - I^\infty_1 \circ \varphi^\infty_{1,0}, J\rangle\big| \\
&\qquad \leq \Big|\big\langle I^n_1, J^n(1,\,\cdot\,) - J^\infty(1,\,\cdot\,)\big\rangle\Big| + \Big|\big\langle I^n_1 - I^\infty_1, J^\infty(1,\,\cdot\,)\big\rangle\Big| \\
&\qquad\qquad \leq \|I^n_1\| \cdot \big\|J^n(1,\,\cdot\,) - J^\infty(1,\,\cdot\,)\big\| + \big|\langle I^n_1 - I^\infty_1, J^\infty(1,\,\cdot\,)\rangle\big|.
\end{aligned}$$

Since $\|I_1^n\|$ is bounded (because $\|\zeta^n\|$ is bounded) and since $I_1^n \rightharpoonup I_1^\infty$ (which we shoed before), all terms above tend to 0 as $n \to \infty$, i.e., (18) holds.

This concludes the proof of (9), which in turn implies the existence of a minimizer of $\mathcal{J}_{\gamma,\tau}(\,\cdot\,; g)$. □

Proposition 5 (Stability)**.** *Let $\{g_k\}_k \subset Y$ and assume this sequence converges (in norm) to some $g \in Y$. Next, for each $\gamma, \tau > 0$ and each k, define $(\boldsymbol{\nu}^k, \zeta^k) \in L^2([0,1], V \times X)$ as*

$$(\boldsymbol{\nu}^k, \zeta^k) = \operatorname*{arg\,min}_{(\boldsymbol{\nu},\zeta)} \mathcal{J}_{\gamma,\tau}(\boldsymbol{\nu}, \zeta; g_k).$$

Then there exists a sub sequence of $(\boldsymbol{\nu}^k, \zeta^k)$ that converges weakly to a minimizer of $\mathcal{J}_{\gamma,\tau}(\,\cdot\,; g)$ in (7).

Proof. We know from proposition 4 that $\mathcal{J}_{\gamma,\tau}(\,\cdot\,; g)$ and $\mathcal{J}_{\gamma,\tau}(\,\cdot\,; g_k)$ has a minimizer for any $g, g_k \in Y$. The idea is first to show that the sequences $(\boldsymbol{\nu}^k)_k$ and $(\zeta^k)_k$ are bounded. Next, we show that there exists a weakly converging subsequence of $(\boldsymbol{\nu}^k, \zeta^k)$ that converges to a minimizer of $\mathcal{J}_{\gamma,\tau}(\,\cdot\,; g)$.

By (7), for each k we have (as $(\boldsymbol{\nu}^k, \zeta^k)$ minimizes $\mathcal{J}_{\gamma,\tau}(\,\cdot\,; g_k)$)

$$\|\boldsymbol{\nu}^k\|_2^2 \le \frac{2}{\gamma}\,\mathcal{J}_{\gamma,\tau}(\,\cdot\,; g_k)(\boldsymbol{\nu}^k, \zeta^k) \le \frac{2}{\gamma}\,\mathcal{J}_{\gamma,\tau}(\,\cdot\,; g_k)(\mathbf{0}, 0)\,. \tag{19}$$

Observe now that if $\boldsymbol{\nu} = \mathbf{0}$ and $\zeta = 0$, then $\varphi_{0,1}^{\boldsymbol{\nu}} = \mathrm{Id}$ by (1) and $I_1^{\boldsymbol{\nu},\zeta} = I_0$ by (6), so in particular

$$\mathcal{W}\big(\varphi_{0,1}^{\boldsymbol{\nu}}, I_1^{\boldsymbol{\nu},\zeta}\big)\big) = I_0 \quad \text{whenever } \boldsymbol{\nu} = \mathbf{0} \text{ and } \zeta = 0,$$

Hence, $\mathcal{J}_{\gamma,\tau}(\,\cdot\,; g_k)(\mathbf{0}, 0) = \mathcal{L}\big(\mathcal{A}(I_0), g_k\big)$ and, in addition, $\|\boldsymbol{\nu}\|_2 = 0$ and $\|\zeta\|_2 = 0$, so (19) becomes

$$\|\boldsymbol{\nu}^k\|_2^2 \le \frac{2}{\gamma}\,\mathcal{L}\big(\mathcal{A}(I_0), g_k\big) \to \mathcal{L}(\mathcal{A}(I_0), g) \quad \text{as } k \to \infty. \tag{20}$$

In conclusion, the sequence $(\boldsymbol{\nu}^k)_k \subset L^2([0,1], V)$ is bounded, so it has a sub sequence that converges weakly to some element $\boldsymbol{\nu}^\infty \in L^2([0,1], V)$. In a similar way, $(\zeta^k)_k \subset L^2([0,1], X)$ is bounded, so it has a sub sequence that converges weakly to some element $\zeta^\infty \in L^2([0,1], X)$.

In order to show that $(\boldsymbol{\nu}^\infty, \zeta^\infty) \in L^2([0,1], V \times X)$ minimizes $\mathcal{J}_{\gamma,\tau}(\,\cdot\,; g)$, we will show that $\mathcal{J}_{\gamma,\tau}(\boldsymbol{\nu}^\infty, \zeta^\infty; g) \le \mathcal{J}_{\gamma,\tau}(\boldsymbol{\nu}, \zeta; data)$ for any $(\boldsymbol{\nu}, \zeta) \in L^2([0,1], V \times X)$.

From the weak convergences, we obtain

$$\begin{aligned}\frac{\gamma}{2}\|\boldsymbol{\nu}^\infty\|_2^2 + \frac{\tau}{2}\|\zeta^\infty\|_2^2 &\le \frac{\gamma}{2}\liminf_k \|\boldsymbol{\nu}^k\|_2^2 + \frac{\tau}{2}\liminf_k \|\zeta^k\|_2^2 \\ &\le \frac{1}{2}\liminf_k \Big[\gamma\|\boldsymbol{\nu}^k\|_2^2 + \tau\|\zeta^k\|_2^2\Big]. \end{aligned} \tag{21}$$

The weak convergence also implies (see proof of proposition 4) that

$$\mathcal{W}(\varphi_{0,1}^k, I_1^\infty) \rightharpoonup \mathcal{W}(\varphi_{0,1}^\infty, I_1^\infty) \quad \text{in } X.$$

In the above, we have used the notational convention introduced in (8). By the lower semi-continuity of $\mathcal{L}$, we get

$$\mathcal{L}\Big(\mathcal{A}\big(\mathcal{W}(\varphi_{0,1}^\infty, I_1^\infty)\big), g\Big) \leq \liminf \mathcal{L}\Big(\mathcal{A}\big(\mathcal{W}(\varphi_{0,1}^k, I_1^k)\big), g_k\Big). \tag{22}$$

As a consequence,

$$\begin{aligned}\mathcal{J}_{\gamma,\tau}(\boldsymbol{\nu}^\infty, \zeta^\infty; g) &= \frac{\gamma}{2}\|\boldsymbol{\nu}^\infty\|_2^2 + \frac{\tau}{2}\|\zeta^\infty\|_2^2 + \mathcal{L}\Big(\mathcal{A}\big(\mathcal{W}(\varphi_{0,1}^\infty, I_1^\infty)\big), g\Big). \\ &\leq \frac{1}{2}\liminf_k \Big[\gamma\|\boldsymbol{\nu}^k\|_2^2 + \tau\|\zeta^k\|_2^2\Big] + \liminf_k \mathcal{L}\Big(\mathcal{A}\big(\mathcal{W}(\varphi_{0,1}^k, I_1^k)\big), g_k\Big) \\ &\leq \liminf_k \mathcal{J}_{\gamma,\tau}(\boldsymbol{\nu}^k, \zeta^k; g_k). \end{aligned} \tag{23}$$

Next, since $(\boldsymbol{\nu}^k, \zeta^k) \in L^2\left([0,1], V \times X\right)$ minimizes $\mathcal{J}_{\gamma,\tau}(\,\cdot\,; g_k)$, we get

$$\mathcal{J}_{\gamma,\tau}(\boldsymbol{\nu}^\infty, \zeta^\infty; g) \leq \liminf_k \mathcal{J}_{\gamma,\tau}(\boldsymbol{\nu}, \zeta; g_k) \quad \text{for any } (\boldsymbol{\nu}, \zeta) \in L^2\left([0,1], V \times X\right).$$

Furthermore, $\mathcal{J}_{\gamma,\tau}(\boldsymbol{\nu}, \zeta; g_k) \to \mathcal{J}_{\gamma,\tau}(\boldsymbol{\nu}, \zeta; g)$, so we conclude that

$$\mathcal{J}_{\gamma,\tau}(\boldsymbol{\nu}^\infty, \zeta^\infty; g) \leq \mathcal{J}_{\gamma,\tau}(\boldsymbol{\nu}, \zeta; data) \quad \text{for all } (\boldsymbol{\nu}, \zeta) \in L^2\left([0,1], V \times X\right).$$

In particular, we have shown that $(\boldsymbol{\nu}^\infty, \zeta^\infty)$ minimises $\mathcal{J}_{\gamma,\tau}(\,\cdot\,; g)$. □

Convergence investigates the behaviour of the solution as data error tends to zero and regularization parameters are adapted accordingly (parameter choice rule) to the data error.

Proposition 6 (Convergence)**.** *Let $g \in Y$. We suppose that there exists $(\hat{\boldsymbol{\nu}}, \hat{\zeta})$ such that $\mathcal{A}\big(\mathcal{W}(\varphi_{0,1}^{\hat{\boldsymbol{\nu}}}, I_1^{\hat{\boldsymbol{\nu}},\hat{\zeta}})\big) = g$. For given $\delta > 0$, we define*

$$(\boldsymbol{\nu}_\delta, \zeta_\delta) \in \operatorname*{arg\,min}_{(\boldsymbol{\nu},\zeta)} \mathcal{J}_{\gamma(\delta),\tau(\delta)}(\boldsymbol{\nu}, \zeta; g + e_\delta)$$

where data error $e_\delta \in Y$ has magnitude $\|e_\delta\| = \delta$. Next, assume there exists parameter choice rules $\delta \mapsto \gamma(\delta)$ and $\delta \mapsto \tau(\delta)$ such that $\delta \mapsto \gamma(\delta)/\tau(\delta)$ and $\delta \mapsto \tau(\delta)/\gamma(\delta)$ are bounded and

$$\lim_{\delta\to 0} \gamma(\delta) = \lim_{\delta\to 0} \tau(\delta) = \lim_{\delta\to 0} \frac{\delta^2}{\gamma(\delta)} = \lim_{\delta\to 0} \frac{\delta^2}{\tau(\delta)} = 0.$$

Then, there exists a subsequence $(\boldsymbol{\nu}_{\delta_k}, \zeta_{\delta_k})$ of $(\boldsymbol{\nu}_\delta, \zeta_\delta)$ such that $\delta_k \to 0$ and $(\boldsymbol{\nu}_{\delta_k}, \zeta_{\delta_k})$ converges weakly towards $(\boldsymbol{\nu}^*, \zeta^*)$ that satisfies $\mathcal{A}\big(\mathcal{W}(\varphi_{0,1}^{\boldsymbol{\nu}^*}, I_1^{\boldsymbol{\nu}^*,\zeta^*})\big) = g$.

Proof. let (δ_k) be a sequence converging to 0 and, for each k, let us denote $g_k = g + e_{\delta_k}$, $\boldsymbol{\nu}_k, = \boldsymbol{\nu}_{\delta_k}$ and $\zeta_k = \zeta_{\delta_k}$.

Similarly to previous proofs, let us show that the sequences $(\boldsymbol{\nu}^k)$ and (ζ^k) are bounded, and then that the weakly converging subsequence that can be extracted from $(\boldsymbol{\nu}^k, \zeta^k)$ converges to a suitable solution. .

Define $\gamma_k := \gamma(\delta_k)$ and $\tau_k := \gamma(\delta_k)$. Then, for each k we have

$$\begin{aligned}|\boldsymbol{\nu}^k|^2 &\leq \frac{1}{\gamma_k}\,\mathcal{J}_{\gamma_k,\tau_k,g_k}(\boldsymbol{\nu}^k,\zeta^k) \leq \frac{1}{\gamma_k}\,\mathcal{J}_{\gamma_k,\tau_k,g_k}(\widehat{\boldsymbol{\nu}},\hat{\zeta}) \\ &= \frac{1}{\gamma_k}\Big(\gamma_k|\widehat{\boldsymbol{\nu}}|^2 + \tau_k|\hat{\zeta}|^2 + \mathcal{L}(g,g_k)\Big) \leq |\widehat{\boldsymbol{\nu}}|^2 + \frac{\tau_k}{\gamma_k}|\hat{\zeta}|^2 + \frac{\delta^k}{\gamma^k}.\end{aligned}$$

From the assumptions on γ, τ, and δ, we conclude that $(\boldsymbol{\nu}^k)$ is bounded in $L^2([0,1],V)$ and similarly one can show that (ζ^k) is bounded. Hence, there is a subsequence of $(\boldsymbol{\nu}^k, \zeta^k)$ that converges weakly to $(\widetilde{\boldsymbol{\nu}}, \widetilde{\zeta})$ in $L^2([0,1],V) \times L^2([0,1],V)$.

Then (see proof of existence of minimizer for $\mathcal{J}_{\gamma,\tau}(\,\cdot\,;g)$)

$$\mathcal{L}\Big(\mathcal{A}\big(\mathcal{W}(\varphi_{0,1}^{\widetilde{\boldsymbol{\nu}}}, I_1^{\widetilde{\boldsymbol{\nu}},\widetilde{\zeta}})\big), g\Big) \leq \liminf \mathcal{L}\Big(\mathcal{A}\big(\mathcal{W}(\varphi_{0,1}^{\boldsymbol{\nu}^k}, I_1^{\widetilde{\boldsymbol{\nu}},\widetilde{\zeta}})\big), g_k\Big).$$

Furthermore, this quantity converges to 0 because for each k:

$$\begin{aligned}\mathcal{L}\Big(\mathcal{A}\big(\mathcal{W}(\varphi_{0,1}^{\boldsymbol{\nu}^k}, I_1^{\boldsymbol{\nu}^k,\zeta^k})\big), g_k\Big) &\leq \mathcal{J}_{\gamma_k,\tau_k,d_k}(\boldsymbol{\nu}^k,\zeta^k) \\ &\leq \mathcal{J}_{\gamma_k,\tau_k,d_k}(\widehat{\boldsymbol{\nu}},\hat{\zeta}) = \gamma_k|\widehat{\boldsymbol{\nu}}|^2 + \tau_k|\hat{\zeta}|^2 + \mathcal{L}(g,g_k)\end{aligned}$$

which tends to 0. Hence, $\mathcal{A}\big(\mathcal{W}(\varphi_{0,1}^{\widetilde{\boldsymbol{\nu}}}, I_1^{\widetilde{\boldsymbol{\nu}},\widetilde{\zeta}})\big) = g$. □

6 Application to 2D tomography

6.1 The inverse problem

We present here several examples of reconstruction from 2D parallel beam tomographic data with our framework and compare these results with other reconstruction methods.

6.2 Framework

We use in the following scalar gaussian kernels

$$K_\sigma(x,y) := \exp\Big(-\frac{|x-y|^2}{2\sigma^2}\Big) \quad \text{for scalar parameter } \sigma > 0.$$

Furthermore, $\mathcal{A}\colon X \to Y$ is the parallel beam ray transform which is a continuous operator. It is sampled at a certain number of angles that will be specified for each case. Finally, $\mathcal{L}$ is the L^2-distance on the range of $\mathcal{A}$.

For each example we will specify following four parameters: the kernel-size σ, the number of angles of the ray transform, and the two regularisation parameters λ and τ defined in (7).

In addition, since data is noisy, we will also specify the signal-to-noise ratio (SNR) defined as

$$\mathrm{SNR}(g) = 10 \log_{10}\left(\frac{\|g_0 - \overline{g_0}\|^2}{\|\eta - \overline{\eta}\|^2}\right) \quad \text{for } g = g_0 + \eta.$$

In the above, g_0 is the noise-free term and η is the noise term in data with $\overline{g_0}$ and $\overline{\eta}$ denoting the mean of g_0 and η, respectively. The SNR is expressed in terms of dB.

The results that we present are obtained by minimising the objective functional in (7) via a gradient descent.

6.3 Multi object and poorly-chosen intensities

We first present the reconstruction we obtain with the same data as in fig. 1: the template and the ground truth image have the same topology but the intensities and shapes of objects are different, see fig. 2. The SNR is here 15.6 dB. The ray transform is here taken with 100 angles and the size kernel is $\sigma = 2$ (the size of the images is 16×16). The reconstructed image is presented in fig. 2(h), and the intermediate trajectories for the metamorphosis are shown in fig. 2 (image, deformation part and template part).

We can see on this example that the metamorphosis indirect registration framework (unlike the LDDMM one, see fig. 1) allows to recover both intensities and geometric changes between the template image and the ground truth. Besides the result can be decomposed into these two variations, enabling easy visual interpretation.

6.4 Object appearance and poorly-chosen intensities

We present here the reconstruction we obtain with Shepp-Logan images where the ground truth image is a deformed Shepp-Logan with a non-uniform background and an additional white disc (see fig. 3). The SNR is here 10.6 dB. The ray transform is here taken with 100 angles and the size kernel is $\sigma = 3$ (the size of the images is 16×16). The reconstructed image is presented in fig. 2(h), and the intermediate trajectories for the metamorphosis are shown in fig. 3 (image, deformation part and template part).

As previously, the ground truth is well reconstructed and one can follow both the deformation of the template and the appearance of the white disc.

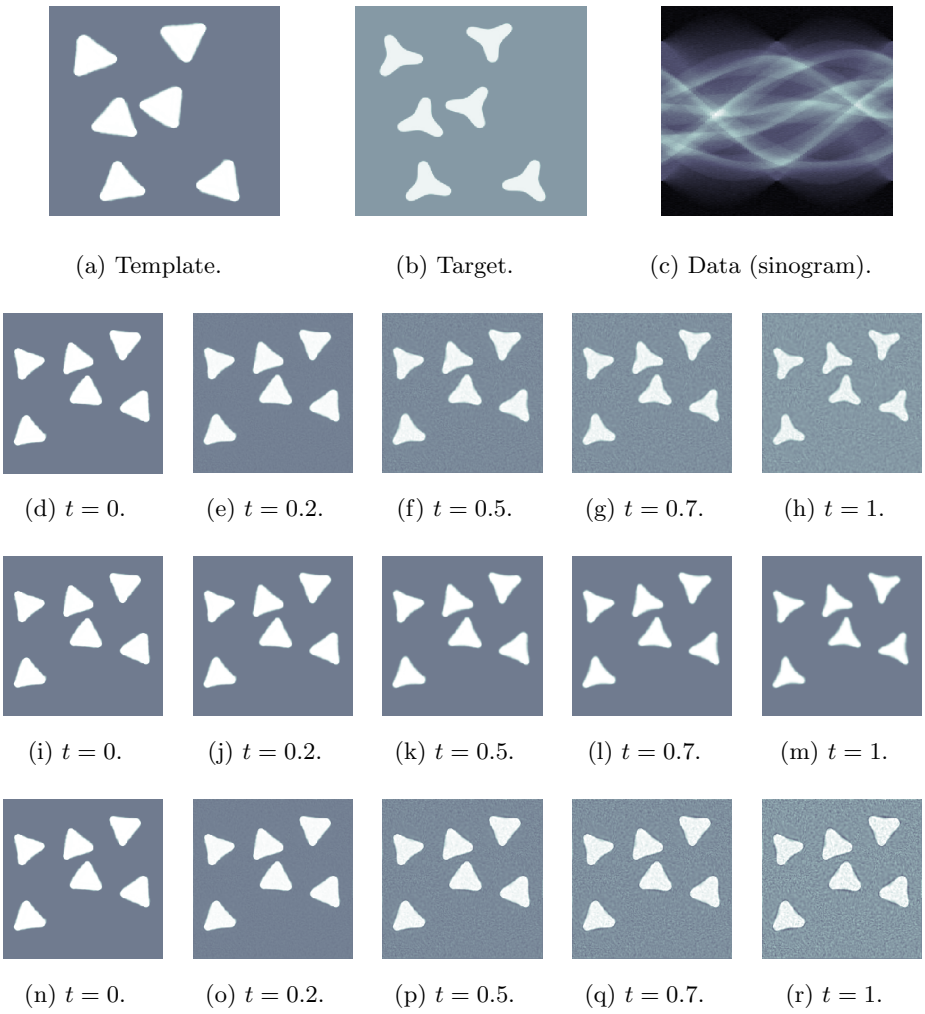

(a) Template. (b) Target. (c) Data (sinogram).

(d) $t = 0$. (e) $t = 0.2$. (f) $t = 0.5$. (g) $t = 0.7$. (h) $t = 1$.

(i) $t = 0$. (j) $t = 0.2$. (k) $t = 0.5$. (l) $t = 0.7$. (m) $t = 1$.

(n) $t = 0$. (o) $t = 0.2$. (p) $t = 0.5$. (q) $t = 0.7$. (r) $t = 1$.

Figure 2: Metamorphosis based indirect-matching of template in (a) against data in (c), which represents 2D ray transform of target in (b) (100 uniformly distributed angles in $[0, \pi]$). The second row (d)–(h) shows the image trajectory $t \mapsto \mathcal{W}(\varphi^{\boldsymbol{\nu}}_{0,t}, f_t(\boldsymbol{\nu}, \zeta))$, so the final registered template is in (h). The third row (i)–(m) shows the deformation trajectory $t \mapsto \mathcal{W}(\varphi^{\boldsymbol{\nu}}_{0,t}, I_0)$, likewise the fourth row (n)–(r) shows the intensity trajectory $t \mapsto f_t(\boldsymbol{\nu}, \zeta)$.

(a) Template I_0.

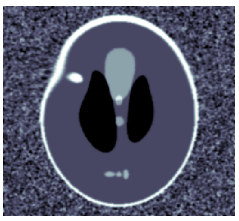

(b) Ground truth.

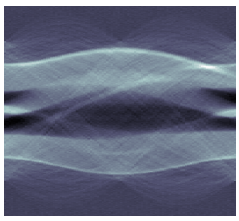

(c) Data (sinogram).

(d) $t = 0$.

(e) $t = 0.2$.

(f) $t = 0.5$.

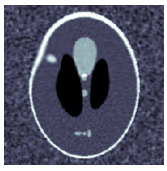

(g) $t = 0.7$.

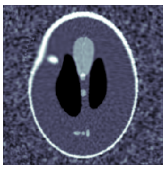

(h) $t = 1$.

(i) $t = 0$.

(j) $t = 0.2$.

(k) $t = 0.5$.

(l) $t = 0.7$.

(m) $t = 1$.

(n) $t = 0$.

(o) $t = 0.2$.

(p) $t = 0.5$.

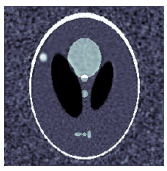

(q) $t = 0.7$.

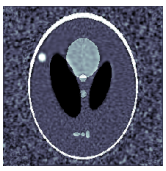

(r) $t = 1$.

Figure 3: Metamorphosis based indirect-matching of template in (a) against data in (c), which represents 2D ray transform of target in (b) (100 uniformly distributed angles in $[0, \pi]$). The second row (d)–(h) shows the image trajectory $t \mapsto \mathcal{W}(\varphi^{\boldsymbol{\nu}}_{0,t}, f_t(\boldsymbol{\nu}, \zeta))$, so the final registered template is in (h). The third row (i)–(m) shows the deformation trajectory $t \mapsto \mathcal{W}(\varphi^{\boldsymbol{\nu}}_{0,t}, I_0)$, likewise the fourth row (n)–(r) shows the intensity trajectory $t \mapsto f_t(\boldsymbol{\nu}, \zeta)$.

6.5 Example of application for spatio-temporal reconstruction

The goal of this framework is to perform spatio-temporal reconstruction, it will be the object of another article but we present here a preliminary result with images of the same type as in section 6.4. Here the acquisition is done at 10 different time points (from $t = 0.1$ to $t = 1$), with an object under study that is moving. Besides we suppose that the acquisition is slow so that for each of the 10 time points, only data for limited angles are available: we suppose that the $i-$th acquisition corresponds to the ray transform with 10 angles randomly distributed between $(i-1)\pi/10$ and $i\pi/10$. The moving ground truth and the obtained results are presented on fig. 4 and examples of data are shown on fig. 5.

We also present in fig. 6, the result of reconstruction we obtained using the TV algorithm and the Filter-back-projection on the concatenation of 10 data (corresponding then to a ray transform with 100 angles). Theses concatenated data are shown on fig. 6(c).

We can see on these figures that, unlike TV and FBP algorithms, our method allows to catch the evolution of the object under study (both the deformation and the appearance of the white disc).

6.6 Robustness

Performing the reconstruction via the framework that we present requires to choose three parameters: the kernel-size σ and the two regularisation parameters λ and τ. We study here the influence of their choices in the reconstruction result of the experiment presented in Section 6.4.

In practice, the reconstruction result, as well as its decomposition in template-part and deformation-part, is not too sensitive to the choice the two regularisation parameters λ and τ. We present in table 1 the structural similarity (SSIM) and peak signal-to-noise ratio (PSNR) values for σ equal to 3 and varying regularisation parameters.

The reconstruction result is more sensitive to the choice of the kernel size. We present in fig. 7 the reconstructed image, and the corresponding final template-part and deformation part for various values of σ. We also give in table 2 the values of SSIM and PSNR of each kernel size. One can see that even if, for all values of the kernel size the reconstruction is satisfying, its decomposition in the template part and deformation part are really different. The deformation and the change in grey-scale value combine sometimes in a non-intuitive way in order to produce a suitable reconstructed image.

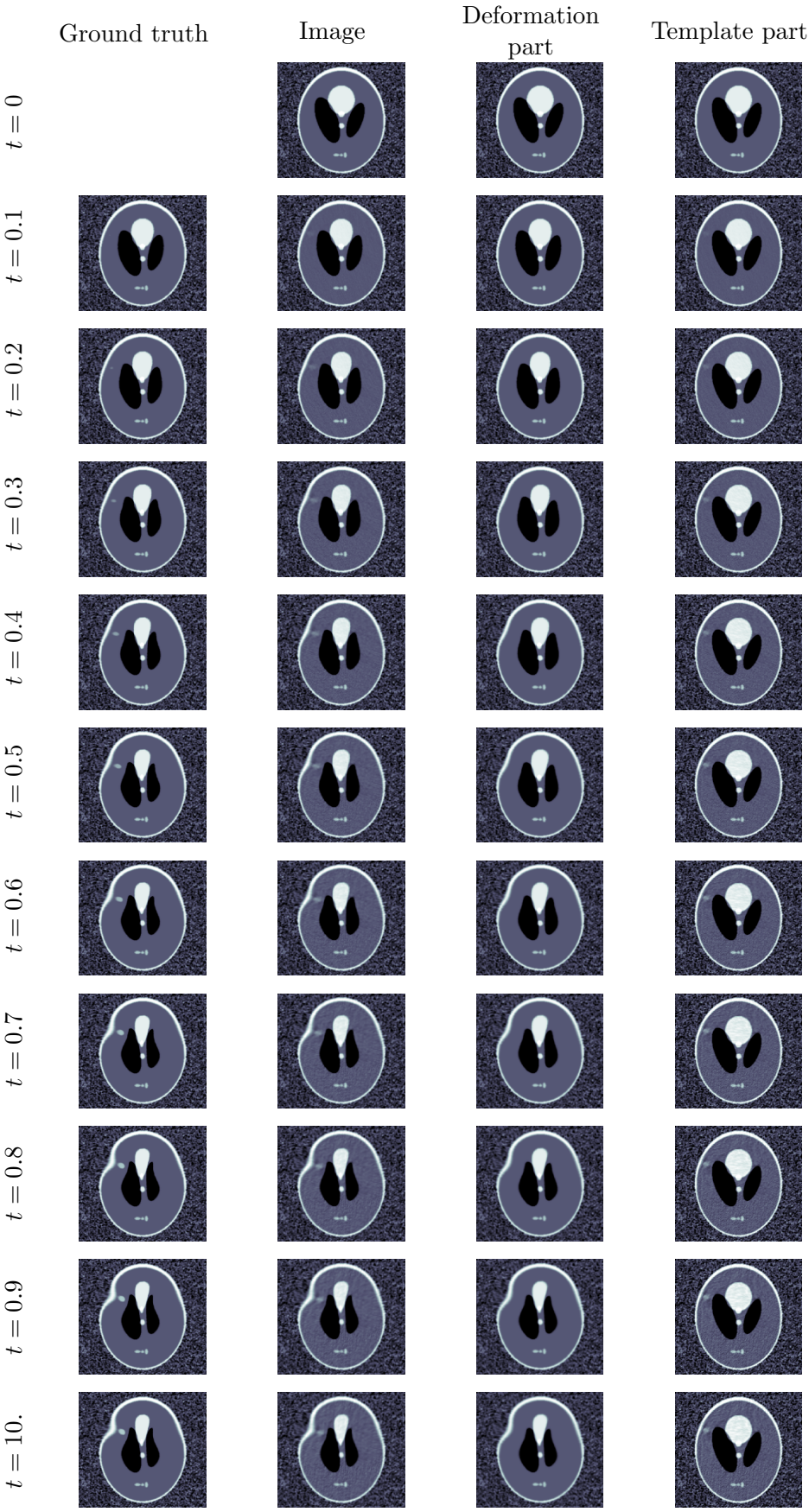

Figure 4: Spatio-temporal reconstruction with Metamorphosis framework, the template is shown at the first row (same initialisation for the Image, template part and deformation part). The first column shows the ground truth images at the 10 data time points; the second column shows the image trajectory (i.e. the reconstructions) $t \mapsto \mathcal{W}(\varphi^{\boldsymbol{\nu}}_{0,t}, f_t(\boldsymbol{\nu}, \zeta))$; the third column shows the deformation trajectory $t \mapsto \mathcal{W}(\varphi^{\boldsymbol{\nu}}_{0,t}, I_0)$; and the fourth column shows the intensity trajectory $t \mapsto f_t(\boldsymbol{\nu}, \zeta)$.

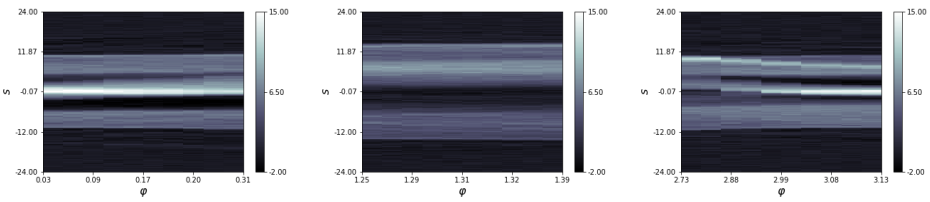

(a) $t = 0.1$. (b) $t = 0.5$. (c) $t = 1$.

Figure 5: Examples of data used for the spatio-temporal reconstruction with Metamorphosis framework.

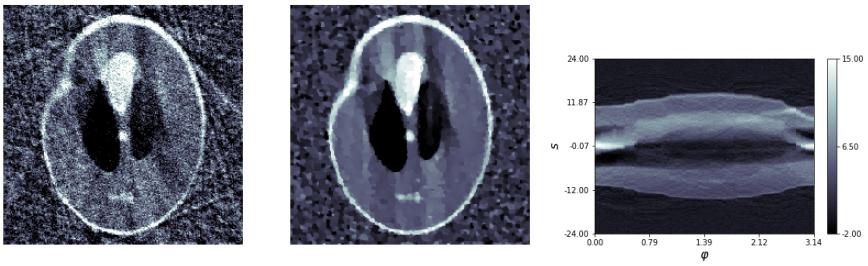

(a) FBP. (b) TV. (c) Concatenated data.

Figure 6: Reconstruction from spatio-temporal data (see fig. 4), methods: FBP (left) and TV (middle).

τ \ γ	10^{-7}	10^{-5}	10^{-3}	10^{-1}
10^{-1}	0.768	0.765	0.765	0.765
	-6.49	-6.62	-6.62	-6.62
10^{-3}	0.768	0.7666	0.7666	0.7666
	-6.39	-6.49	-6.49	-6.49
10^{-5}	0.768	0.7666	0.7666	0.7666
	-6.39	-6.49	-6.49	-6.49
10^{-7}	0.768	0.7666	0.7666	0.7666
	-6.39	-6.49	-6.49	-6.49

Table 1: SSIM (top) and PSNR (bottom) values for Metamorphosis-indirect-matching reconstruction with varying regularisation parameter and $\sigma = 3$ for several regularisation parameters.

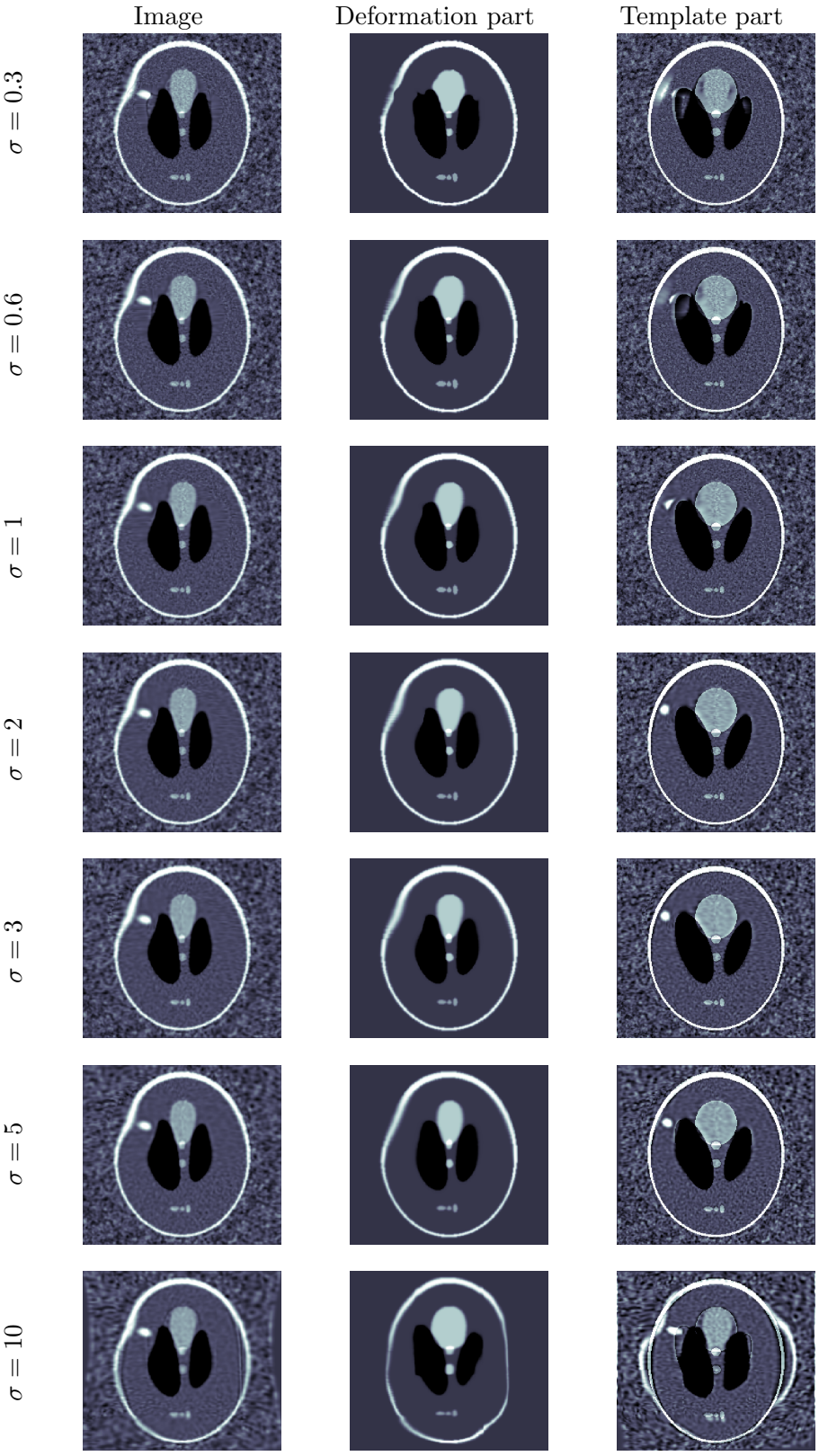

Figure 7: Reconstruction results and their recomposition in template part and deformation part for various kernel size σ.

σ	0.3	0.6	1	2	3	5	10
SSIM	0.640	0.89	0.737	0.769	0.766	0.764	0.681
PSNR	-8.12	-7.30	-6.58	-6.34	-6.49	-6.67	-8.99

Table 2: SSIM and PSNR values for Metamorphosis-indirect-matching reconstruction with varying kernel size σ and fixed regularisation parameters $\lambda = \tau = 10^{-5}$.

7 Survey of spatiotemporal reconstruction methods in nuclear medical imaging

7.1 Gating

The conventional approach to account for motion is through independent frame-by-frame reconstruction. Here data is gated, i.e., sub-divided into sub-sets that represent data acquired when the organs at the same specific temporal state. For cardiac and respiratory motion, gated data would correspond to decomposition of the whole dataset into parts that represent different breathing and/or cardiac phases. After gating each single gate shows less motion, however, suffers from a relatively low signal-to-noise ratio as only a small portion of all available events is contained. Reconstruction is then performed, one for each temporal state using the associated sub-set of gated data. In this way, 4D reconstruction problem is reduced to a sequence of independent 3D reconstruction problems. In this context one often speaks of double gated data, which is when there are two sources of motion, e.g., motion of the beating heart and respiratory motion of the lungs and thoracic wall.

Gating techniques that account for the beating heart are usually based on using a electrocardiogram (shows the heart as it contracts over the interval from one R wave to the next) to guide data acquisition. Gating techniques that account for respiratory motion are more challenging, e.g., optical tracking systems are used to measure the respiratory motion, see survey in [7] for an overview. These are mostly engineering considerations, a research topic of interest is to consider computational gating, i.e., computationally 'freeze' the movement to overcome motion artefacts. One example is optical gating techniques that exploit the periodic motion of the heart [95].

7.2 Organ motion models

The topics listed here deal with motion models for organs, which in turn is closely related to image registration and shape analysis. Emphasis is on cardiac and respiratory motion, see [26, 81, 31] for nice surveys of this topic.

Cardiac motion Many cardiac motion models are developed to provide diagnostic information about the cardiac function.

Physics-based deformable models can be used to parameterise deformations that captured the motion of the left ventricle [73]. 4D B-splines can also be used to interpolate the motion between the tracked myocardial points [72]. The 4D displacement field formed by combining the 2D fields, as derived from the short-axis and long-axis image planes, could be used to track the deformation of points anywhere within the myocardium. These models are estimated from tagged magnetic resonance imaging (MRI) images of the

heart, but the deformation model itself may be of relevance also for cardiac PET/computed tomography (CT) and SPECT/CT imaging.

Another approach, which is used when the motion model is estimated from other imaging modalities, is based on extensions of the classic optical flow approach of [42]. The optical flow technique assumes that a moving point in a sequence of images does not change its intensity. The classic approach invokes local Taylor series approximations (using partial derivatives with respect to the spatial and temporal coordinates). It was first applied directly to 2D cardiac images in [61, 1]. Because 2D motion is inadequate to describe cardiac motion vectors, extension to the 3D setting is given in [90, 104] on CT cardiac sequences.

One may also consider motion models inspired from linear elastic material models as in [49, 23]. Here, the motion field is regularised by an energy function constraining the source volume as if it were a physical elastic material being deformed by external forces. Yet another approach is based on the optical flow method [36], which assume that a moving point in a sequence of images does not change its intensity. This assumption may be violated in emission tomography because of the limited spatial resolution (and the resulting partial volume effect), particularly as the myocardium expands and becomes thin in the end-diastolic phase. An alternative is to invoke the continuity equation describing conservation of mass (here, intensity), resulting in an additional term relative to classic optical flow (and sometimes referred to as extended optical flow) [90]. See also [50] which proposes a technique based on 3D optical flows combined with a model of the myocardium as an elastic membrane.

Respiratory motion Respiratory motion of the heart, if unaccounted for, may introduce imaging artefacts that resemble false defects [59]. Furthermore, it also introduces considerable degradations in quantitative accuracy of images [79] and quality of polar maps [74].

A central topic in this context is rigid versus non-rigid modelling of the motion. Respiratory motion of the heart (as well as liver, stomach, spleen, and kidneys) do for the most part involve rigid translations downward and to the interior as the diaphragm contracts during inspiration [89, 53]. Nonetheless, such motion also induces non-rigid movements (deformations) of the heart, as it is pushed and pulled by the diaphragm and other connected tissue [2]. Quantitative measures reveal that non-rigid motion was close to 10% in several cases [51]. On the other hand, only small improvements were observed [51] after performing non-rigid motion modelling. Hence, whether to use a rigid or non-rigid model depends on the resolution of the PET scanner.

The simplest non-rigid motion model is affine, which has six parameters (3D rotation and translation). One may extend the affine model to a rigid

model that also allow three scale [56] and three skew parameters [51]. An approach for non-rigid modelling based on optical flows is reported in [24]. A regularised B-spline approach with a Markov random field regulariser is used in [5], see also [21].

Other shape-constrained deformable models that have specifically been developed for organ segmentation in 3D medical images are surveyed in [99], see also [29] for a survey of shape models in the context of emission tomography. Registration and segmentation techniques for pulmonary image analysis are provided in [86] and [68, 81, 31] surveys respiratory motion correction strategies and deformation models relevant for thoracic PET, PET/CT that are also applicable to SPECT. Finally, we also mention [48] which is the largest evaluation of non-linear deformation algorithms applied to brain image registration ever conducted. Many of these are also relevant in the context of 4D PET and SPECT.

7.3 Reconstruction methods that incorporate motion

Traditional reconstruction methods for inverse problems with temporal variation is frame-by-frame reconstruction (assumes gated data), followed by extracting the temporal behaviour of the objects or regions of interest through curve fitting and other image-based processing. In such an approach, one only exploits the spatial relationship between the image to be recovered and the measurement data at each time instant. Hence, one does not account for the temporal dynamics of the underlying process, leading to non-optimal results unless the solution is temporally uncorrelated.

The term 4D reconstruction refers to methods that seek to account for the temporal dynamics in the 3D images. Several approaches have recently been proposed, see [25, 81, 85, 31] for surveys (some of these references also deal with integrating temporal models for the radiotracer kinetics into the reconstruction scheme, but the methods should also work with temporal models for organ motion). In order to keep the radiation burden as low as possible, most methods estimated motion model parameters on basis of the PET or SPECT data instead of, e.g., gated CT images. They can be classified into four groups [5]:

(i) Averaging of aligned images (inter-iterative temporal smoothing).

(ii) Re-reconstruction using a time-varying forward model.

(iii) Event re-binning.

(iv) Joint reconstruction of image and motion.

All but the last category requires that a motion model is estimated prior to reconstruction. See also [69] for a survey of effects of motion, attenuation, and scatter corrections on gated cardiac SPECT reconstruction. This

paper investigate how these degrading factors will impact the reconstructed myocardium for different reconstruction methods.

Averaging of aligned images After gating the data, each gate is reconstructed individually and aligned to one assigned reference gate. To overcome the problem of low signal-to-noise rations, the aligned images are averaged (summed) afterwards using an estimated motion model, which provides motion vectors that enables tracking any given voxel across the gates. One may here use any of the motion models listed in section 7.2.

Such an approach was suggested in [10] for cardiac gated data. One may also in the reconstruction replace the uniform-voxel framework by a mesh [11]. This provides an efficient image description based on non-uniform sampling as mesh nodes are placed more densely in image regions having finer detail. However, the investigators seem to have abandoned this approach in favour of post-reconstruction motion-compensated filtering in later publications [64, 12]. Overall, spatial [43, 67] or temporal [46, 83] inter-iteration filtering methods are ad hoc (e.g., are not proved to be convergent).

Re-reconstruction using a time-varying forward model Similar to item i, data is gated and each individually reconstructed gate is aligned to one assigned reference gate. The obtained motion information is incorporated into a subsequent re-reconstruction of the whole dataset by incorporating the motion field into the linear forward model.

Approaches along this line focus mostly on integrating motion models into the forward model within the maximum-likelihood expectation maximisation (ML-EM) method, see [57, 28] for respiratory motion correction approaches in PET and [15] for SPECT. Most approaches are based on modifying the maximum a posteriori (MAP)-OSL algorithm of [39], e.g., [38] uses a formulation to encourage smoothing across the gated frames. Furthermore, [36, 37] provides a generalised weighted formulation to weight inter-gate variations in voxel intensities depending on gate separation (higher weights for nearer gates), see also [54, 55] for a similar approach.

Event re-binning An issue with the approaches item i and item ii above is that they treat the same moving image as different temporal reconstructions that are merely temporally correlated. A truly 4D approach would estimate deformations and incorporate these within a unified forward model.

In PET one may gate the acquired list mode data and reconstruct each gate. Motion is estimated based on these reconstructed images. The initial list mode data is re-binned in a subsequent step by applying the transformation gained from the motion estimation step. Such an approach was proposed and investigated in [78, 58, 56] for respiratory gating applications, which later was also used for cardiac gating [93]. The measured non-rigid

motion (estimated from the gated images) is modelled in the image-space and becomes part of the forward model resulting in a truly 4D ML-EM reconstruction algorithm, see also [41, 66, 82].

An alternative is to incorporate a motion model in the reconstruction procedure since it does not modify data and thereby preserve its statistical properties. This is proposed in [77] (rigid) and [78] (rigid and non-rigid). The work in [78, 77] is extended in [71] to describe a reconstruction algorithm specifically tailored to list-mode PET data containing motion signals (e.g., from MR navigators) along with detected coincidences. In this approach, all counts are reconstructed into one reference frame in order to maximise signal-to-noise ratio, while correcting for motion, in order to minimise motion blurring. This method can be easily extended to motion-corrected, frame-by-frame dynamic reconstruction.

Joint reconstruction of image and motion Here, motion is estimated simultaneously to the reconstruction of the image. An objective function is optimised w.r.t. two arguments: image and motion. Hence, only one image with the full statistic is reconstructed. Given the close link between the image reconstruction and motion estimation steps, a simultaneous method of estimating the two is better able to reduce motion blur and compensate for poor signal-to-noise ratios and to improve the accuracy of the estimated motion [33, 36]. A draw-back is the relatively high computational costs involved in such a joint reconstruction approach.

In [33, 36] one seeks to perform a two-step minimization of a joint energy functional term (which included both image likelihood and motion-matching terms). This work was also extended from a two-frame approach to the complete cardiac cycle in [34]. See also [62, 73, 18] for algorithms that include similar regularisation via the strain energy function for the purpose of myocardium motion estimation. The approach taken by Jacobson and Fessler [44, 45] considered a parametric Poisson model for gated PET measurements involving the activity distribution as unknown as well as a set of deformation parameters describing the motion of the image throughout the scan (from gate to gate). By maximising the log-likelihood for this model, a technique referred to as joint estimation with deformation modelling was used to determine both the image and deformation parameter estimates jointly from the full set of measured data. A similar motion-aware likelihood function is used in [9], although using a distinct optimisation scheme and depicting more convincing results. In his context one may also consult [103], which compares three approaches for joint reconstruction of image and motion: a state-space model, the separability condition and a multiple constraints model. By formulating these methods in a common statistical regularisation framework, the authors are able to illuminate their relationships.

A common model for double gated data is to model the respiratory

motion of the heart as rigid. One can then transform individual lines of response (i.e., via translations and rotations) to compensate for respiratory motion, followed by standard reconstructions of individual cardiac-gated datasets [60]. This approach does not compensate for duration of time each line of response spends outside the field-of-view because of motion, which can be compensated via multiplication factors applied to the motion-compensated events [16] or by modifying the sensitivity images through the 4D ML-EM formalism. The latter approach is taken in [79, 21] where 4D respiratory motion is compensated for each cardiac phase. It is also possible to pursue 4D reconstruction methods that incorporate both cardiac and respiratory gating information as in [9] that uses data from a dual-gated framework with 24 total gates. Nonetheless, in practice, the common approach has been to use 4D reconstruction methods to compensate for respiratory motion within each cardiac gate, followed by post-reconstruction registration and summing of cardiac-gated images [21, 94].

A novel approach to incorporate correction for cardiac and pulmonary motion in dual gated PET/CT cardiac imaging is provided in [32]. Intensity modulations caused by the highly non-rigid cardiac motion are considered by means of a mass-preserving transformation model initially developed for image registration [17, 65]. This motion model is incorporated into a variational regularisation framework for joint motion estimation and reconstruction. See also [13] for a variational regularisation for joint reconstruction of image and motion in which the motion is modelled by mass conservation and [87] for a variational approach to joint reconstruction of image and motion in SPECT. Another alternative is to consider motion models derived from LDDMM based deformations. Finally, [27] provides an overview of variational shape models as applied to the registration and segmentation problems. These could also be coupled with variational regularisation methods for image reconstruction. One may also consider microlocal analysis for recovering moving edges in CT given an estimated model for motion [47]. This can in turn be used to define dynamic edge based priors for variational 4D combined modality imaging, such as 4D PET/CT and SPECT/CT.

Finally, an important aspect is also how to acquire attenuation maps for cardiac SPECT in the presence of respiratory motion. A comparison of several methods is provided in [52] and see also [75] for attenuation correction in (4D) PET using phase-correlated 4D CT.

7.4 Dynamic dictionaries

The central theme here is to develop 4D dictionaries for 3D images with temporal variation. Sparse representations for video restoration (denoising [76, 63] and in-painting [63]) are examples of dictionaries that encode both spatial and temporal information. Dictionary learning methods can be applied to dynamic imaging scenarios, see [4] for dynamic MRI. Here, the

spatio-temporal data, and thereby the spatio-temporal dictionary atoms, exhibit joint coherence in space and time.

For analytic dictionaries, the feasibility of wavelet-based compression of 4D images with smooth grey scale variations is shown in [101] for ultrasound images, see also where 4D ultrasound images of the beating heart are compressed about 2000 times without impairing upon the diagnostic usability [30, 102, 92]. In the context of 4D PET, there are dictionaries that encode spatial and temporal variability [84]. The approach is to estimate both a set of temporal basis functions and the corresponding coefficient for each basis function at each spatial location within the image. The joint estimation is performed through a fully 4D version of the ML-EM algorithm. Results are compared to the conventional frame-by-frame independent reconstruction with ML-EM for varying levels of both spatial and temporal post-reconstruction smoothing. Another similar approach is developed in [97], see also [80]. As of writing, there is however no transform based dictionary providing a sparse representation of edge information over time. Here, one could use techniques from [47] to develop a 4D variant of shearlets for sparse representation of spatio-temporal images.

References

[1] S. C. Amartur and H. J. Vesselle. A new approach to study cardiac motion: the optical flow of cine MR images. *Magnetic Resonance in Medicine*, 29(1):59—67, 1993.

[2] K. Andersen and H. Vik-Mo. Effects of spontaneous respiration on left ventricular function assessed by echocardiography. *Circulation*, 69(5):874–879, 1984.

[3] S. Arguillere, E. Trélat, A. Trouvé, and L. Younes. Shape deformation analysis from the optimal control viewpoint. *Journal de mathématiques pures et appliquées*, 2015.

[4] S. Awate and E. DiBella. Spatiotemporal dictionary learning for undersampled dynamic MRI reconstruction via joint frame-based and dictionary-based sparsity. In *2012 9th IEEE International Symposium on Biomedical Imaging (ISBI)*, pages 318–321, 2012.

[5] W. Bai and M. Brady. Motion correction and attenuation correction for respiratory gated PET images. *IEEE Transactions on Medical Imaging*, 30(2):351—365, 2011.

[6] M. Bertero, H. Lantéri, and L. Zanni. Iterative image reconstruction: a point of view. In Y. Censor, M. Jiang, and A. K. Louis, editors, *Proceedings of the Interdisciplinary Workshop on Mathematical Methods in Biomedical Imaging and Intensity-Modulated Radiation (IMRT), Pisa, Italy*, pages 37–63, 2008.

[7] V. Bettinardi, E. De Bernardi, L. Presotto, and M. C. Gilardi. Motion-tracking hardware and advanced applications in PET and PET/CT. *PET Clinics*, 8(1):11–28, 2013.

[8] E. Bladt, D. M. Pelt, S. Bals, and K. J. Batenburg. Electron tomography based on highly limited data using a neural network reconstruction technique. *Ultramicroscopy*, 158:81–88, 2015.

[9] M. Blume, A. Martinez-Moller, A. Keil, N. Navab, and M. Rafecas. Joint reconstruction of image and motion in gated positron emission tomography. *IEEE Transactions on Medical Imaging*, 29(11):1892—1906, 2010.

[10] J. G. Brankov, Y. Yang, M. V. Narayanan, and M. N. Wermck. Motion-compensated 4D processing of gated SPECT perfusion studies. In *IEEE Nuclear Science Symposium Conference Record, 2002. Norfolk (VA), November 10–16, 2002*, pages 1380–1384, 2002.

[11] J. G. Brankov, Y. Yang, and M. N. Wernick. Tomographic image reconstruction based on a content-adaptive mesh model. *IEEE Transactions on Medical Imaging*, 23(2):202—212, 2004.

[12] J. G. Brankov, Y. Yang, and M. N. Wernick. Spatiotemporal processing of gated cardiac SPECT images using deformable mesh modeling. *Medical Physics*, 32(9):2839—2849., 2005.

[13] C. Brune. *4D Imaging in Tomography and Optical Nanoscopy*. PhD thesis, University of Münster, 2010.

[14] M. Bruveris and D. D. Holm. Geometry of image registration: The diffeomorphism group and momentum maps. In *Geometry, Mechanics, and Dynamics*, pages 19–56. Springer, 2015.

[15] P. P. Bruyant, M. A. King, and P. H. Pretorius. Correction of the respiratory motion of the heart by tracking of the center of mass of thresholded projections: a simulation study using the dynamic MCAT phantom. *IEEE Transactions on Nuclear Science*, 49(5):2159—2166, 2002.

[16] P. Bühler, U. Just, E. Will, J. Kotzerke, and J. van den Hoff. An accurate method for correction of head movement in PET. *IEEE Transactions on Medical Imaging*, 23(9):1176–1185, 2004.

[17] M. Burger, J. Modersitzki, and L. Ruthotto. A hyperelastic regularization energy for image registration. *SIAM Journal on Scientific Computing*, 35(1):B132–B148, 2013.

[18] Z. Cao, D. R. Gilland, B. A. Mair, and R. J. Jaszczak. Three-dimensional motion estimation with image reconstruction for gated cardiac ECT. *IEEE Transactions on Nuclear Science*, 50(3):384–388, 2003.

[19] N. Charon, B. Charlier, and A. Trouvé. Metamorphoses of functional shapes in sobolev spaces. *Foundations of Computational Mathematics*, pages 1–62, 2016.

[20] C. Chen and O. Öktem. Indirect image registration with large diffeomorphic deformations. *SIAM Journal of Imaging Sciences*, 11(1):575–617, 2018.

[21] S. Chen, P. Bravo, M. Lodge, and B. M. W. Tsui. Four-dimensional PET image reconstruction with respiratory and cardiac motion compensation from list-mode data. *Journal of Nuclear Medicine*, 53(1):106, 2012.

[22] G. E. Christensen, R. D. Rabbitt, and M. I. Miller. Deformable template model using large deformation kinematics. *IEEE Transactions on Image Processing*, 5(10):1435–1447, 1996.

[23] S. Y. Chun and J. A. Fessler. Noise properties of motion-compensated tomographic image reconstruction methods. *IEEE Transactions on Medical Imaging*, 32(2):141–152, 2013.

[24] M. Dawood, F. Buther, X. Jiang, and K. P. Schäfers. Respiratory motion correction in 3-D PET data with advanced optical flow algorithms. *IEEE Transactions on Medical Imaging*, 27(8):1164–1175, 2008.

[25] M. Dawood, X. Jiang, and K. P. Schäfers, editors. *Correction Techniques in Emission Tomography.* Series in Medical Physics and Biomedical Engineering. CRC Press, 2008.

[26] J. Ehrhardt and C. Lorenz, editors. *4D Modeling and Estimation of Respiratory Motion for Radiation Therapy.* Biological and Medical Physics, Biomedical Engineering. Springer-Verlag, 2013.

[27] A. A. Farag, A. Shalaby, H. A. El Munim, and A. Farag. Variational shape representation for modeling, elastic registration and segmentation. In S. Li and J. M. T. S. Tavares, editors, *Shape Analysis in Medical Image Analysis*, volume 14 of *Lecture Notes in Computational Vision and Biomechanics*, chapter 95–122. Springer-Verlag, 2014.

[28] L. Fin, P. Bailly, J. Daouk, and M.-E. Meyer. Motion correction based on an appropriate system matrix for statistical reconstruction of respiratory-correlated pet acquisitions. *Computer Methods and Programs in Biomedicine*, 96(3):e1—e9, 2009.

[29] F. Gao and P. Shi. Shape analysis in molecular imaging. In S. Li and J. M. T. S. Tavares, editors, *Shape Analysis in Medical Image Analysis*, volume 14 of *Lecture Notes in Computational Vision and Biomechanics*, chapter 51–93. Springer-Verlag, 2014.

[30] J.-U. Garbas, U. Fecker, T. Troger, and A. Kaup. 4D scalable multiview video coding using disparity compensated view filtering and motion compensated temporal filtering. In *2006 IEEE 8th Workshop on Multimedia Signal Processing, 3–6 October 2006 in Victoria, BC*, pages 54–58, 2006.

[31] F. Gigengack, X. Jiang, M. Dawood, and K. P. Schäfers. *Motion Correction in Thoracic Positron Emission Tomography.* Springer-Verlag, 2015.

[32] F. Gigengack, L. Ruthotto, M. Burger, C. H. Wolters, X. Jiang, and K. P. Schäfers. Motion correction in dual gated cardiac PET using mass-preserving image registration. *IEEE Transactions on Medical Imaging*, 31(3):698–712, 2012.

[33] D. R. Gilland, B. A. Mair, J. E. Bowsher, and R. J. Jaszczak. Simultaneous reconstruction and motion estimation for gated cardiac ECT. *IEEE Transactions in Nuclear Science*, 49(5):2344—2349, 2002.

[34] D. R. Gilland, B. A. Mair, and J. Sun. Joint 4D reconstruction and motion estimation in gated cardiac ECT. In *Proceedings of the International Meeting on Fully Three-Dimensional Image Reconstruction in Radi- ology and Nuclear Medicine. Salt Lake City (UT), July 6–9, 2005*, pages 303—306, 2005.

[35] M. Grasmair. Generalized bregman distances and convergence rates for non-convex regularization methods. *Inverse Problems*, 26(11):115014, 2010.

[36] E. Gravier, Y. Yang, M. A. King, and M. Jin. Fully 4D motion-compensated reconstruction of cardiac SPECT images. *Physics in Medicine and Biology*, 51(18):4603—4619., 2006.

[37] E. Gravier, Y. Y. Yang, and M. W. Jin. Tomographic reconstruction of dynamic cardiac image sequences. *IEEE Transactions on Image Processing*, 16(4):932—942, 2007.

[38] E. J. Gravier and Y. Yang. Motion-compensated reconstruction of tomographic image sequences. *IEEE Transactions in Nuclear Science*, 52(1):51—56, 2005.

[39] P. J. Green. Bayesian reconstructions from emission tomography data using a modified EM algorithm. *IEEE Transactions on Medical Imaging*, 9(1):84–93, 1990.

[40] G. T. Gullberg, B. W. Reutter, A. Sitek, J. S. Maltz, and T. F. Budinger. Dynamic single photon emission computed tomography – basic principles and cardiac applications. *Physics in Medicine and Biology*, 55:R111–R191, 2010.

[41] T. J. Hebert and R. M. Leahy. Fast methods for including attenuation in the EM algorithm. *IEEE Transactions in Nuclear Science*, 37(2):754—758, 1990.

[42] B. K. Horn and B. G. Schunck. Determining optical flow. *Artificial Intelligence*, 17(1–3):185—203, 1981.

[43] M. Jacobson, R. Levkovitz, A. Ben-Tal, K. Thielemans, T. Spinks, D. Belluzzo, E. Pagani, V. Bettinardi, M. C. Gilardi, A. Zverovich, and G. Mitra. Enhanced 3D PET OSEM reconstruction using inter-update Metz filtering. *Physics in Medicine and Biology*, 45(8):2417—2439, 2000.

[44] M. W. Jacobson and J. A. Fessler. Joint estimation of image and deformation parameters in motion-corrected PET. In *2003 IEEE Nuclear Science Symposium Conference Record*, pages 3290—3294, 2003.

[45] M. W. Jacobson and J. A. Fessler. Joint estimation of respiratory motion and activity in 4D PET using CT side information. In *3rd IEEE International Symposium on Biomedical Imaging: Nano to Macro. Arlington, VA, April 6–9, 2006*, pages 275—278, 2006.

[46] D. J. Kadrmas and G. T. Gullberg. 4D maximum a posteriori reconstruction in dynamic SPECT using a compartmental model-based prior. *Physics in Medicine and Biology*, 46(5):1553—1574, 2001.

[47] A. Katsevich. Motion compensated local tomography. *Inverse Problems*, 24(4):045012, 2008.

[48] A. Klein, J. Andersson, B. A. Ardekani, J. Ashburner, B. Avants, M.-C. Chiang, G. E. Christensen, L. Collins, J. Gee, P. Hellier, J. H. Song, M. Jenkinson, C. Lepage, D. Rueckert, T. Thompson, P. Vercauteren, R. P. Woods, J. J. Mann, and V. P. Ramin. Evaluation of 14 nonlinear deformation algorithms applied to human brain MRI registration. *NeuroImage*, 46:786—802, 2009.

[49] G. J. Klein and R. H. Huesman. Four-dimensional processing of deformable cardiac PET data. *Medical Image Analysis*, 6(1):29—46, 2002.

[50] G. J. Klein and R. H. Huesman. Four dimensional processing of deformable cardiac PET data. *Medical Image Analysis*, 1(2002):29–46, 6.

[51] G. J. Klein, R. W. Reutter, and R. H. Huesman. Four-dimensional affine registration models for respiratory-gated PET. *IEEE Transactions in Nuclear Science*, 48(3):756—760, 2001.

[52] A. Könik, J. Kikut, R. Lew, K. Johnson, and M. A. King. Comparison of methods of acquiring attenuation maps for cardiac SPECT in the presence of respiratory motion. *Journal of Nuclear Cardiology*, 20(6):1093–1107, 2013.

[53] H. W. Korin, R. L. Ehman, S. J. Riederer, J. P. Felmlee, and R. C. Grimm. Respiratory kinematics of the upper abdominal organs — a quantitative study. *Magnetic Resonance in Medicine*, 23(1):172—178, 1992.

[54] D. S. Lalush, C. Lin, and B. M. W. Tsui. A priori motion models for four-dimensional reconstruction in gated cardiac SPECT. In *IEEE Nuclear Science Symposium Conference Record, 1996. Anaheim (CA), November 2–9, 1996*, pages 1923–1927, 1996.

[55] D. S. Lalush and B. M. W. Tsui. Block-iterative techniques for fast 4D reconstruction using a priori motion models in gated cardiac SPECT. *Physics in Medicine and Biology*, 43(4):875—886, 1998.

[56] F. Lamare, T. Cresson, J. Savean, C. C. Le Rest, A. J. Reader, and D. Visvikis. Respiratory motion correction for PET oncology applications using affine transformation of list mode data. *Physics in Medicine and Biology*, 52(1):121–140, 2007.

[57] F. Lamare, M. J. Ledesma Carbayo, T. Cresson, G. Kontaxakis, A. Santos, C. C. Le Rest, A. J. Reader, and D. Visvikis. List-mode-based reconstruction for respiratory motion correction in PET using non-rigid body transformations. *Physics in Medicine and Biology*, 52(17):5187–5204, 2007.

[58] T. Li, B. Thorndyke, E. Schreibmann, Y. Yang, and L. Xing. Model-based image reconstruction for four-dimensional PET. *Medical Physics*, 35(5):1288–1298, 2006.

[59] L. Livieratos, K. Rajappan, L. Stegger, K. P. Schäfers, D. L. Bailey, and P. G. Camici. Respiratory gating of cardiac PET data in list-mode acquisition. *European Journal of Nuclear Medicine and Molecular Imaging*, 33(5):584—588, 2006.

[60] L. Livieratos, L. Stegger, P. M. Bloomfield, K. P. Schäfers, D. L. Bailey, and P. G. Camici. Rigid-body transformation of list-mode projection data for respiratory motion correction in cardiac PET. *Physics in Medicine and Biology*, 50(14):3313–3322, 2005.

[61] G. E. Mailloux, A. Bleau, M. Bertrand, and R. Petitclerc. Computer analysis of heart motion from two-dimensional echocardiograms. *IEEE Transactions on Biomedical Engineering*, 34(5):356—364, 1987.

[62] B. A. Mair, D. R. Gilland, and J. Sun. Estimation of images and nonrigid deformations in gated emission CT. *IEEE Transactions on Medical Imaging*, 25(9):1130–1144, 2006.

[63] J. Mairal, G. Sapiro, and M. Elad. Learning multiscale sparse representations for image and video restoration. *SIAM Multiscale Modelling and Simulation*, 7(1):214—241, 2008.

[64] T. Marin and J. G. Brankov. Deformable left-ventricle mesh model for motion-compensated filtering in cardiac gated SPECT. *Medical Physics*, 37(10):5471—5481, 2010.

[65] J. Modersitzki. *FAIR: Flexible Algorithms for Image Registration*. Fundamentals of Algorithms. SIAM, Philadelphia, 2009.

[66] E. U. Mumcuoglu, R. M. Leahy, S. R. Cherry, and et al. Fast gradient-based methods for bayesian reconstruction of transmission and emission PET images. *IEEE Transactions on Medical Imaging*, 13(4):687–701, 1994.

[67] S. Mustafovic and K. Thielemans. Object dependency of resolution in reconstruction algorithms with inter-iteration filtering applied to PET data. *IEEE Transactions on Medical Imaging*, 23(4):433–446, 2004.

[68] S. A. Nehmeh. Respiratory motion correction strategies in thoracic PET-CT imaging. *PET Clinics*, 8(1):29–36, 2013.

[69] X. Niu, Y. Yang, M. Jin, M. N. Wernick, and M. A. King. Effects of motion, attenuation, and scatter corrections on gated cardiac SPECT reconstruction. *Medical Physics*, 38(12):6571–6584, 2011.

[70] O. Öktem, C. Chen, N. O. Domaniç, P. Ravikumar, and C. Bajaj. Shape based image reconstruction using linearised deformations. *Inverse Problems*, 33(3):035004, 2017.

[71] J. Ouyang, Q. Li, and G. El Fakhri. MR-based motion correction for PET imaging. *Seminars in Nuclear Medicine*, 43(1):60–67, 2013.

[72] C. Öztürk and E. R. McVeigh. Four-dimensional b-spline based motion analysis of tagged MR images: introduction and in vivo validation. *Physics in Medicine and Biology*, 45(6):1683–1702, 2000.

[73] J. Park, D. Metaxas, and A. A. Young. Deformable models with parameter functions for cardiac motion analysis from tagged MRI data. *IEEE Transactions on Medical Imaging*, 15(3):278—289, 1996.

[74] M. J. Park, S. Chen, T. S. Lee, G. S. K. Fung, M. Lodge, and B. M. W. Tsui. Generation and evaluation of a simultaneous cardiac and respiratory gated Rb-82 PET simulation. In *IEEE Nuclear Science Symposium and Medical Imaging Conference (NSS/MIC). Valencia, Spain, October 23–29, 2011*, pages 3327–3330, 2011.

[75] F. Pönisch, C. Richter, U. Just, and W. Enghardt. Attenuation correction of four dimensional (4D) PET using phase-correlated 4D-computed tomography. *Physics in Medicine and Biology*, 53(13):N259–N268, 2008.

[76] M. Protter and M. Elad. Image sequence denoising via sparse and redundant representations. *IEEE Transactions on Image Processing*, 18(1):27—36, 2009.

[77] J. Qi and R. H. Huesman. List mode reconstruction for PET with motion compensation: A simulation study. In *Proceedings. 2002 IEEE International Symposium on Biomedical Imaging, 2002.*, pages 413–416, 2002.

[78] F. Qiao, T. Pan, J. W. Clark, and O. R. Mawlawi. A motion-incorporated reconstruction method for gated PET studies. *Physics in Medicine and Biology*, 51:3769–3783, 2006.

[79] A. Rahmim, J. Tang, M. R. Ay, and F. M. Bengel. 4D respiratory motion-corrected Rb-82 myocardial perfusion PET imaging. In *IEEE Nuclear Science Symposium Conference Record. Knoxville, TN, 30 October - 6 November, 2010*, pages 3312—3316, 2010.

[80] A. Rahmim, J. Tang, and H. Zaidi. Four-dimensional (4D) image reconstruction strategies in dynamic PET: beyond conventional independent frame reconstruction. *Medical Physics*, 36(8):3654–3670, 2009.

[81] A. Rahmim, J. Tang, and H. Zaidi. Four-dimensional image reconstruction strategies in cardiac-gated and respiratory- gated PET imaging. *PET Clinics*, 8(1):51–67, 2013.

[82] A. J. Reader, S. Ally, F. Bakatselos, R. Manavaki, R. J. Walledge, A. P. Jeavons, P. J. Julyan, S. Zhao, D. L. Hastings, and J. Zweit. One-pass list-mode EM algorithm for high-resolution 3-D PET image reconstruction into large arrays. *IEEE Transactions in Nuclear Science*, 49(3):693–699, 2002.

[83] A. J. Reader, J. C. Matthews, F. C. Sureau, C. Comtat, R. Trebossen, and I. Buvat. Iterative kinetic parameter estimation within fully 4D PET image reconstruction. In *IEEE Nuclear Science Symposium Conference Record. San Diego, CA, 29 October - 4 November, 2006*, pages 1752—1756., 2006.

[84] A. J. Reader, F. C. Sureau, C. Comtat, R. Trébossen, and I. Buvat. Joint estimation of dynamic PET images and temporal basis functions using fully 4D ML-EM. *Physics in Medicine and Biology*, 51(21):5455–5474, 2006.

[85] A. J. Reader and J. Verhaeghe. 4D image reconstruction for emission tomography. *Physics in Medicine and Biology*, 59(22):R371–R418, 2014.

[86] A. Schmidt-Richberg. *Registration Methods for Pulmonary Image Analysis. Integration of Morphological and Physiological Knowledge*. Aktuelle Forschung Medizintechnik. Springer-Verlag, 2014.

[87] H. Schumacher, J. Modersitzki, and B. Fischer. Combined reconstruction and motion correction in SPECT imaging. *IEEE Transactions in Nuclear Science*, 56:73–80, 2009.

[88] A. Schwarz and M. Leach. Implications of respiratory motion for the quantification of 2D MR spectroscopic imaging data in the abdomen. *Physics in Medicine and Biology*, 45(8):2105—2116, 2000.

[89] W. P. Segars, S. Mori, G. T. Y. Chen, and B. M. W. Tsui. Modeling respiratory motion variations in the 4D NCAT phantom. In *Nuclear Science Symposium Conference Record, 2007. NSS '07. IEEE*, pages 2677—2679, 2007.

[90] S. M. Song and R. M. Leahy. Computation of 3-D velocity fields from 3-D cine CT images of a human heart. *IEEE Transactions on Medical Imaging*, 10(3):295—306, 1991.

[91] A. Sotiras, C. Davatzikos, and N. Paragios. Deformable medical image registration: A survey. *IEEE Transactions on Medical Imaging*, 32(7):1153–1190, 2013.

[92] N. H. Stefansson, K. W. Eliceiri, C. F. Thomas, A. Ron, R. DeVore, R. Sharpley, and J. G. White. Wavelet compression of three-dimensional time-lapse biological image data. *Microscopy and Microanalysis*, 11(9—17), 2005.

[93] J. Tang, F. M. Bengel, and A. Rahmim. Cardiac motion-corrected quantitative dynamic Rb-82 PET imaging. *Journal of Nuclear Medicine*, 51(Suppl 2):123, 2010.

[94] J. Tang, N. Hall, and A. Rahmim. MRI assisted motion correction in dual-gated 5D myocardial perfusion PET imaging. In *2012 IEEE Nuclear Science Symposium and Medical Imaging Conference (NSS/MIC)*, pages 4054–4057, 2012.

[95] J. M. Taylor. Optically gated beating-heart imaging. *Frontiers in Physiology*, 11(5):481, 2014.

[96] A. Trouvé and L. Younes. Metamorphoses through lie group action. *Foundations of Computational Mathematics*, 5(2):173–198, 2005.

[97] J. Verhaeghe, D. Van de Ville, I. Khalidov, Y. D'Asseler, I. Lemahieu, and M. Unser. Dynamic PET reconstruction using wavelet regularization with adapted basis functions. *IEEE Transactions on Medical Imaging*, 27(7):943–959, 2008.

[98] Y. Wang, E. Vidan, and G. Bergman. Cardiac motion of coronary arteries: Variability in the rest period and implications for coronary MR angiography. *Radiology*, 213(3):751—758, 1999.

[99] J. Weese, I. Wächter-Stehle, L. Zagorchev, and J. Peters. Shape-constrained deformable models and applications in medical imaging. In S. Li and J. M. T. S. Tavares, editors, *Shape Analysis in Medical Image Analysis*, volume 14 of *Lecture Notes in Computational Vision and Biomechanics*, chapter 151–184. Springer-Verlag, 2014.

[100] L. Younes. *Shapes and Diffeomorphisms*, volume 171 of *Applied Mathematical Sciences*. Springer-Verlag, 2010.

[101] L. Zeng, C. Jansen, M. A. Unser, and P. Hunziker. Extension of wavelet compression algorithms to 3D and 4D image data: exploitation of data coherence in higher dimensions allows very high compression ratios. In A. F. Laine, M. A. Unser, and A. Aldroubi, editors, *SPIE Proceedings. Wavelets: Applications in Signal and Image Processing IX, 427 (December 5, 2001)*, volume 4478, pages 427–433, 2001.

[102] L. Zhang, C. Vazquez, J. T. Wa, and D. Wang. Zerotree data structure for 4D wavelet coefficient coding. In *2008 IEEE International Conference on Multimedia and Expo, June 23 2008-April 26 2008 in Hannover*, pages 737–740, 2008.

[103] Y. Zhang, A. Ghodrati, and D. H. Brooks. An analytical comparison of three spatio-temporal regularization methods for dynamic linear inverse problems in a common statistical framework. *Inverse Problems*, 21(1):357–382, 2005.

[104] Z. Y. Zhou, C. E. Synolakis, R. M. Leahy, and S. M. Song. Calculation of 3D internal displacement-fields from 3D x-ray computer tomographic-images. *Proceeding of the Royal Society of London A: Mathematical and Physical Sciences*, 449(1937):537—554, 1995.